

COMBINATORIAL INVESTIGATION OF THE EFFECTS OF  
SODIUM ON  $\text{Cu}_2\text{ZnSnSe}_4$  POLYCRYSTALLINE THIN FILMS

by

Alex Hilton Gibbs

A thesis submitted to the faculty of  
The University of Utah  
in partial fulfillment of the requirements for the degree of

Master of Science

Department of Materials Science and Engineering

The University of Utah

August 2016

Copyright © Alex Hilton Gibbs 2016

All Rights Reserved

# The University of Utah Graduate School

## STATEMENT OF THESIS APPROVAL

The thesis of Alex Hilton Gibbs

has been approved by the following supervisory committee members:

Michael A. Scarpulla, Chair 01/14/2016  
Date Approved

Taylor Sparks, Member 01/14/2016  
Date Approved

Ling Zang, Member 01/15/2016  
Date Approved

and by Feng Liu, Chair/Dean of

the Department/College/School of Materials Science and Engineering

and by David B. Kieda, Dean of The Graduate School.

## ABSTRACT

Cu<sub>2</sub>ZnSnSe<sub>4</sub> (CZTSe) possess highly suitable optical and electronic properties for use as an absorber layer in thin film solar cells. CZTSe also has potential to achieve terawatt level solar energy production due to its inexpensive and abundant material constituents. Currently, fabricating CZTSe devices with the expected theoretical performance has not been achieved, making the growth and formation of CZTSe an interesting topic of research. In this work, a two-step vacuum fabrication process consisting of RF co-sputtering followed by reactive annealing was explored as a viable technique for synthesizing CZTSe thin films. Furthermore, the enhancement of the fabrication process by the incorporation of sodium during annealing was studied using a combinatorial approach. Film composition was analyzed using electron dispersive spectroscopy. Structure, phase morphology, and formation were determined using scanning electron microscopy, x-ray diffraction, atomic force microscopy and raman spectroscopy. Optical and electronic properties were characterized using UV-Vis and Voc were measurements under a one sun solar simulator.

RF co-sputtering CuSe, ZnSe, and SnSe precursors produced films with good thickness uniformity, adhesion and stoichiometry control over 3 x 3 in<sup>2</sup> substrates. Composition measurements showed that the precursor films maintained stability during an annealing process of 580° C for 20 minutes producing near stoichiometric CZTSe. However, grain size was small with an average diameter of 350 nm. The CZTSe film

produced by this process exhibited a suitable absorption coefficient of  $> 10^4 \text{ cm}^{-1}$  and a band gap near 1.0 eV. The film also produced an XRD pattern consistent with tetragonal CZTSe with no secondary phase formation with the exception of approximately 12.5 nm of interfacial  $\text{MoSe}_2$  formation at the back contact.

The combinatorial investigation of the influence of sodium on CZTSe growth and morphology was achieved using a custom built constant withdraw shutter to evaporate NaF with a 0-60 nm thickness spread on the substrate prior to precursor sputtering. This experiment showed that the incorporation of NaF did enhance grain size; however, there was little correlation with initial NaF composition observed. It is concluded that NaF undergoes a high degree of vapor transport and readily distributes nonuniformly throughout the film during the annealing process and also potentially escapes the annealing environment if not properly contained. An experiment on achieving Na incorporation by diffusion from a soda lime glass substrate resulted in a far more uniform enhancement of grain growth. The experiment also revealed that NaF greatly reduced precursor film adhesion to the substrate due to the hygroscopic nature of NaF. X-ray diffraction measurements also showed that the addition of the NaF layer could potentially suppress the formation of  $\text{MoSe}_2$ .

## TABLE OF CONTENTS

ABSTRACT.....	iii
LIST OF FIGURES .....	vi
LIST OF TABLES .....	ix
Chapters	
1. INTRODUCTION AND MOTIVATION .....	1
2. BACKGROUND .....	5
2.1 The Photovoltaic Effect .....	5
2.2 Thin Film Solar Cell Structure.....	8
2.3 CZTSe Absorber Layer.....	11
2.4 CZTSe Fabrication: Sputtering.....	12
2.5 CZTSe: Fabrication Annealing.....	14
2.6 Incorporation of Sodium .....	17
2.7 Combinatorial Analysis .....	18
3. EXPERIMENTAL PROCEDURES.....	19
3.1 CZTSe Thin Film Fabrication.....	19
3.2 NaF Thickness Gradient Deposition.....	22
4. RESULTS AND DISCUSSION .....	26
4.1 Energy-dispersive X-ray Spectrometry Calibration.....	26
4.2 Chemical and Structural Results.....	27
4.3 NaF Doping Analysis: Delamination.....	34
4.4 NaF Doping Analysis: Structure and Electronic Properties .....	37
5. CONCLUSION.....	47
REFERENCES .....	50

## LIST OF FIGURES

Figures	Page
1.1 2014 materials cost for competing thin film photovoltaic absorber layers. Data from the U.S. Geological Survey January 2015. ....	4
1.2 2014 materials cost for competing thin film photovoltaic absorber layers. Data from the U.S. Geological Survey January 2015 .....	4
2.1 Schematic of solar cell operation upon photon absorption.....	6
2.2 Measured intensity of solar spectrum at Earth's surface vs photon energy.....	6
2.3 Plot of equation (1) and (2): Current-Voltage of ideal diode model of a solar cell in dark and illuminated .....	7
2.4 Cross-sectional View of typical thin film solar cell structure.....	9
2.5 Shockly-Queisser limit on theoretical efficiency with respect to absorber layer band gap .....	10
2.6 Crystal structure for both CIGS and CZTSSe with cation substitution.....	11
2.7 Image of co-sputtering target configuration used in this study.....	13
2.8 Plot of PSe <sub>2</sub> vs T for each binary chalcogen precursor oxidation state transition. At an annealing temperature of 580 oC a vapor pressure of 2 Pa is required to stabilize SnIVSe <sub>2</sub> .....	16
2.9 Illustration of a combinatorial deposition using a robotically controlled shutter. Films A and B are deposited with a linear thickness gradient to give a full range of composition across substrate .....	18
3.1 Deposition rate vs power trends for the three binary selenide targets .....	21
3.2 Graphite box base containing 3x3 in <sup>2</sup> substrate surrounded by a recess where selenium pellets are placed .....	22

3.3	Image of automatic constant withdrawal shutter used to deposit NaF thickness gradient for combinatorial analysis (evaporation source below not imaged). ....	23
3.4	NaF film with thickness gradient prior to loading into sputtering chamber for CuSe-ZnSe-SnSe deposition.....	25
3.5	Thickness measurements taken along the length of the gradient (lower). Slope of line shows an approximate reduction in thickness of 1.3 nm/mm across substrate. ....	25
4.1	SEM images of blisters caused by trapped Ar during sputtering with corresponding EDS results.....	28
4.2	SEM and EDS results of fabricated CZTSe thin film.....	29
4.3	X-ray diffraction pattern of CZTSe film showing only minor MoSe <sub>2</sub> secondary phase formation.....	30
4.4	Figure 4.4: Raman spectra data detecting the major peaks of CZTSe at 193 cm <sup>-1</sup> and 233 cm <sup>-1</sup> .....	32
4.5	Optical characteristics of CZTSe film used for band gap and absorption coefficient calculation. %Transmission and Reflectance. ....	33
4.6	absorption coefficient and Tauc plot showing band gap estimation.....	33
4.7	Demonstration of the dramatic effects water has on NaF treated precursors .....	35
4.8	Images of scribe marks demonstrating the impact underlying NaF film has on film adhesion.....	36
4.9	SEM images of grain size taken every 3 mm along the NaF composition gradient .....	38
4.10	SEM image of cross section of CZTSe film doped with NaF gradient .....	38
4.11	Backscattered electron image of Na treated CZTSe with corresponding EDS. The image shows that the large surface grains are most likely the same phase as the underlying surface. Spot EDS data shows little difference in stoichiometry with the exception of less Se in large surface grains. ....	39
4.12	Comparison of XRD patterns from CZTSe treated with NaF (green) and without NaF (blue) showing the suppression of MoSe <sub>2</sub> (blue arrows) .....	40
4.13	Images of NaF doped films after CdS/ITO deposition).....	41



4.14	Voc measurements taken along the NaF composition gradient.....	42
4.15	SEM image of CZTSe sample fabricated on soda lime glass substrate. Image shows larger and more uniform grain growth compared to CZTSe sample fabricated on sodium free eagle glass with NaF precursor layer .....	43
4.16	Illustration of face to face annealing technique preventing Na vapor loss .....	43
4.17	Image of CZTSe film doped with NaF gradient annealed “face to face” with another identical sample. The labels A-E correspond to the different spectral regions.....	43
4.18	SEM and EDS results for each spectral region A-E as labeled in Fig 4.14. These results show a dramatic increase in grain size and grain density from the edges towards the center regions .....	44
4.19	Plot of atomic ratios for each spectral region labeled in Fig. 4.14. It can be seen that Zn/Sn ratios remain nearly constant around 0.9 while Se content decrease from 1.6 at the edge to 1.1 in the center.....	45

## LIST OF TABLES

Tables	Page
1.1 Literature values for the Gibbs free energy of relevant reactions.....	15
4.1 RBS Data of CZTSe Standard Compared to EDS Results .....	27

## CHAPTER 1

### INTRODUCTION AND MOTIVATION

As human civilization continues to expand into the 21<sup>st</sup> century, so do the challenges associated with global power production. In 2012, the world consumed an estimated 17.7 TW ( $1.77 \times 10^{13}$  W) of power which is projected to increase 56% by 2040 [1]. Continuing to meet this growing power demand has prompted increasing concern over the limited supply and environmental impact of fossil fuels, which account for 85% of the world's energy production [2]. This has motivated a shift towards energy production from clean, renewable technologies such as wind, solar, and hydroelectric. Among these technologies, solar power has gained considerable attention for having the potential for terawatt (TW) level power production. With approximately 23,000 TW of solar energy arriving at the earth's surface every year, only a miniscule amount would need to be converted to supply the world's energy needs. Despite this potential, only 177 GW of solar power was generated in 2014, signifying the need for further progress in photovoltaic(PV) research to increase the feasibility of solar power [3].

One of the largest challenges with TW level solar power production is the large surface area and therefore the amount of material required. The peak solar irradiance on the earth's surface is measured to be approximately  $1 \text{ kW/m}^2$  [4], and assuming 10% efficient solar panels, it would require  $10,000 \text{ km}^2$  or 1.3% the area of Texas to generate

1 TW of power. Given this, basic criteria for reducing the cost of solar power technologies are to minimize cell thickness/volume, optimize solar energy conversion efficiency, minimize manufacturing cost, and utilize cheap and abundant materials.

Solar cell modules based on a variety of materials have been developed in pursuit of satisfying these three criteria. Crystalline silicon (Si) modules, which currently accounts for 91% of the PV market, have maintained the greatest success in achieving a competitive price [4]. Silicon is cheap and abundant and advancements in silicon wafer fabrication have led to the development of large-scale manufacturing processes that produce high efficient cells with economies of scale price reduction. However, crystalline silicon is a weak absorber so the majority of the cost is confined to the price of high-quality Si substrates that have to be several hundred micrometers thick to optimally absorb the solar spectrum of light.

Inorganic thin film solar cells have emerged as a commercially competitive technology by achieving high efficiencies with minimal cell thickness. Utilizing semiconductors with high absorption coefficients ( $>10^4 \text{ cm}^{-1}$ ), thin film solar cells only need to be on the order of several microns thick to optimally absorb light. In addition, thin film technology enables rapid, large surface area fabrication and can utilize a wide range of substrates such as glass, metal foil, and plastic. The thin film PV industry is dominated by technologies based on CdTe and  $\text{Cu}_2\text{InGaSe}_2$  (CIGS) which have demonstrated record cell efficiencies exceeding 21%, closely approaching that of crystalline silicon. However, the high cost and low abundance of tellurium, indium, and gallium pose limitations on the scale up potential of these thin film solar technologies and currently only constitute 9% of the total PV market [5].

Further attempts to realize the full scale up potential of thin film PV has developed a promising substitute for CIGS made from cheap, earth abundant materials. By replacing the expensive and rare group III elements contained in CIGS with zinc and tin yields  $\text{Cu}_2\text{ZnSn}(\text{S}_x\text{Se}_{1-x})_4$  (CZTSSe). The potential for price reduction with CZTSSe can be seen in Fig. 1.1 and 1.2 which compare the materials price and production rate of CZTSSe to CIGS and CdTe. The close similarities in structure and optoelectronic properties to CIGS give CZTSSe the potential to achieve similar device performance and serve as a drop-in substitute in the CIGS manufacturing process. The current demonstrated record efficiency for CZTSSe is 12.6% [6], 9.6% [7] for the pure selenide compound CZTSe and 8.4% [8] for the pure sulfur compound CZTS. These efficiencies are still far below what is needed for CZTSSe to be commercially viable and finding ways to improving these numbers is an ongoing topic of research.

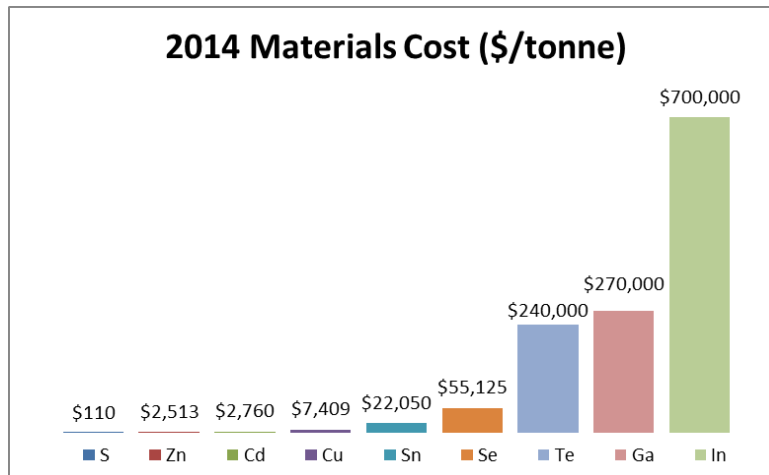


**Figure 1.1:** 2014 materials cost for competing thin film photovoltaic absorber layers. Data from the U.S. Geological Survey January 2015

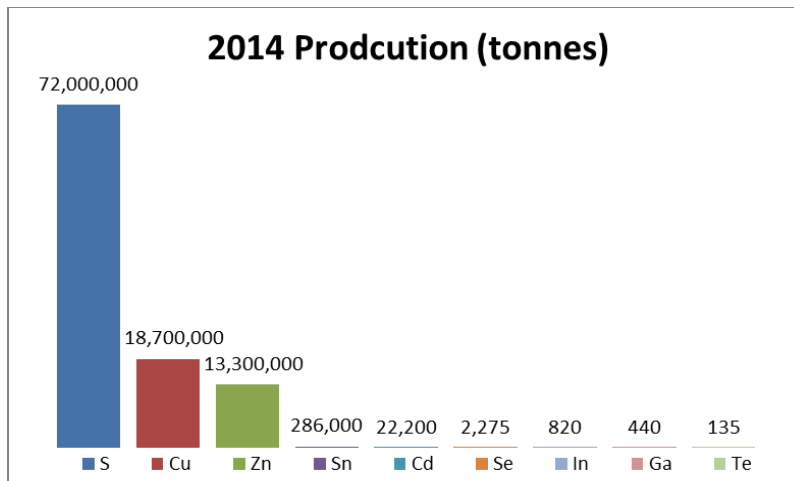


**Figure 1.2:** 2014 materials cost for competing thin film photovoltaic absorber layers. Data from the U.S. Geological Survey January 2015

## CHAPTER 2

### BACKGROUND

#### 2.1 The Photovoltaic Effect

A solar cell can be defined as quantum particle converter which converts a photon current into an electron current. This conversion process is achieved by a process called the photovoltaic effect where a voltage is generated within a semiconductor upon exposure to light. When a photon of energy  $E_{ph} = hv_{ph}$  is absorbed in a semiconductor with a band gap energy  $E_g \leq E_{ph}$ , electron-hole pair charge carriers are generated and can diffuse through the material. Forming a contact junction consisting of a semiconductor with p-type conductivity and a semiconductor with n-type conductivity forms a built in potential difference at the junction. Electron-hole pairs that do not recombine with the lattice before reaching the junction can be separated by the electric field provided by the built in potential. This separation will result in the accumulation of excess carriers on both sides of the p-n junction which generates a voltage that can drive a current through an external circuit as depicted in Fig. 2.1.

Examining the solar spectrum in Fig. 2.2, it can be seen that the sun's intensity peaks within the range of 0.5 eV to 3 eV which corresponds to the visible (3 eV to 1.7 eV) and infrared [9]. Approximately 94-98% of the sun's energy is within this range and semiconductors with band gap in the infrared are used in solar cells in order to absorb this

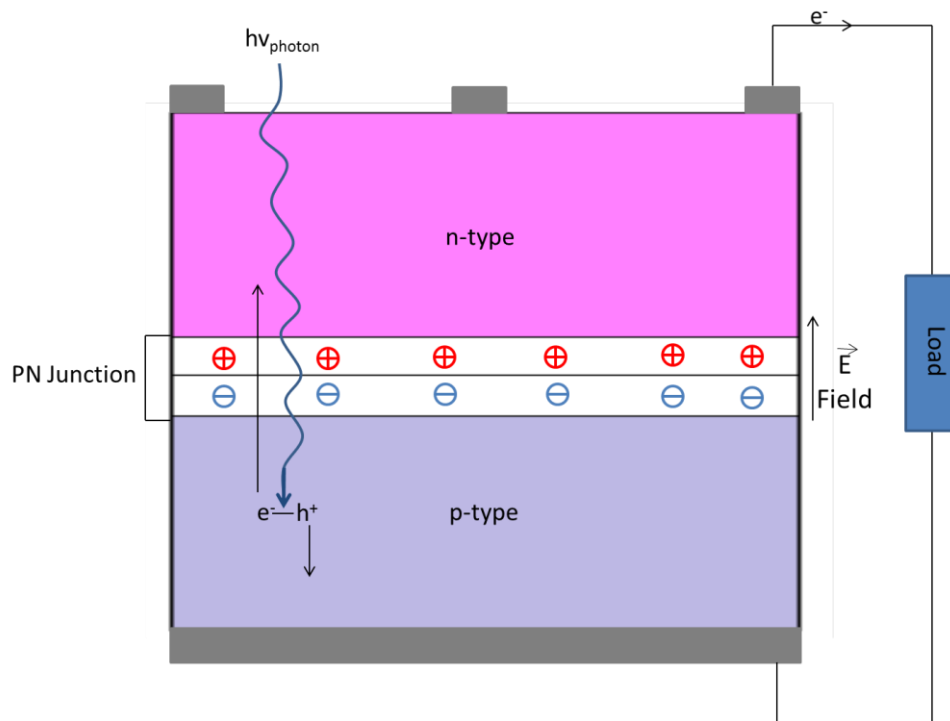


**Figure 2.1:** Schematic of solar cell operation upon photon absorption

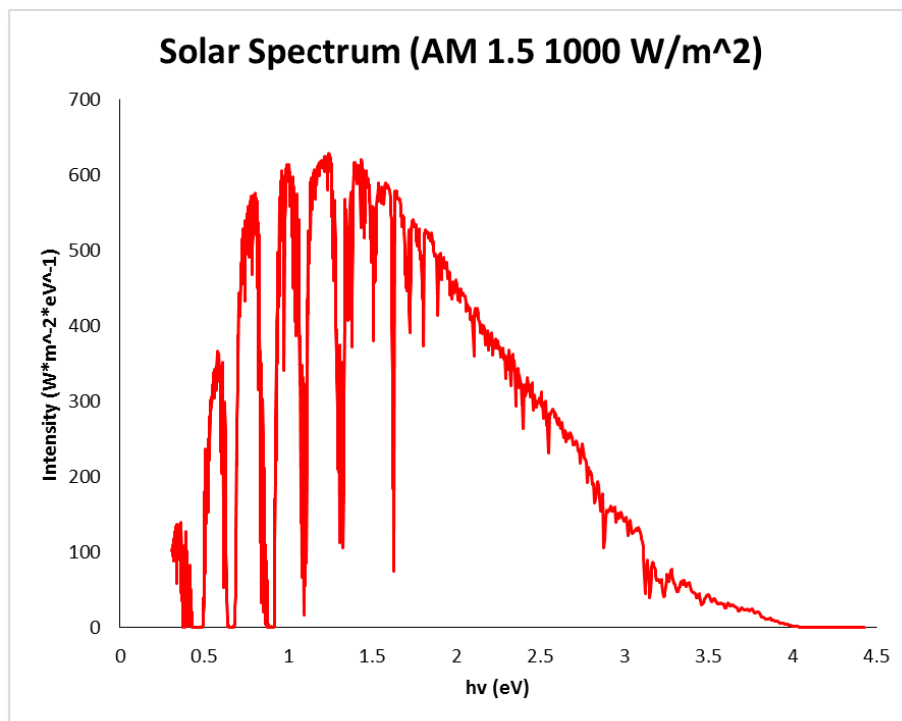


**Figure 2.2:** Measured intensity of solar spectrum at Earth's surface vs photon energy



range of energies [10].

Describing the voltage generated in a photovoltaic cell in terms of excess carrier concentration can be done by treating the photovoltaic cell as an ideal diode. The current-voltage characteristics of an ideal diode in the dark are modeled using the ideal diode equation:

$$J = J_o \left[ \exp\left(\frac{qV}{kT}\right) - 1 \right] \quad (1)$$

where  $J_o$  is the reverse dark saturation current density. When the solar cell is illuminated, a light generated current ( $J_L$ ) is created and results in a superposition of the total current in equation (1):

$$J = J_o \left[ \exp\left(\frac{qV}{kT}\right) - 1 \right] - J_L \quad (2)$$

Equations (1) and (2) are plotted in Fig. 2.3. From equation (2), the voltage at open circuit can be obtained by setting  $J = 0$ :

$$V_{oc} = \left(\frac{kT}{q}\right) \ln \left[ \frac{J_L}{J_o} + 1 \right] \quad (3)$$

The efficiency of a photovoltaic cell can then be calculated from the fill factor (FF) and total power in ( $P_{in}$ ):

$$\eta = \frac{V_{oc} J_{sc} FF}{P_{in}} \quad (4)$$

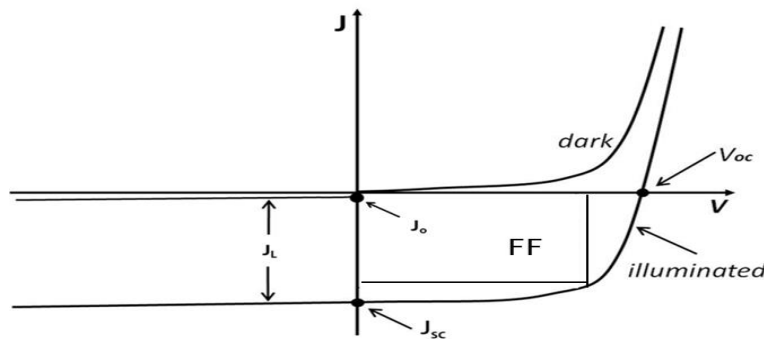


**Figure 2.3:** Plot of equation (1) and (2): Current-Voltage of ideal diode model of a solar cell in dark and illuminated

When a solar cell is under constant illumination, a steady state balance between the incoming photon current and the electron recombination current is maintained:

$$J_L = J_{rec} \quad (5)$$

This balance generates excess electron density  $\Delta n$  within the material. Assuming a constant generation rate  $G$ , the recombination current density can be written as:

$$J_{rec} = qGL = \frac{q\Delta nL}{\tau_{eff}} = J_L \quad (6)$$

where  $L$  is the thickness of the material and  $\tau_{eff}$  is the effective carrier life time. The reverse saturation current  $J_o$  is dependent on the quality of the material and is a measure of the recombination in a solar cell by the following relation considering a p-type absorber layer:

$$J_o = \frac{qn_i^2L}{\tau_{eff}(N_A + \Delta n)} \quad (7)$$

where  $n_i$  is the intrinsic carrier concentration and  $N_A$  is the dopant concentration.

Inserting equations (6) and (7) into equation (3) yields an equation which establishes a relationship between  $V_{oc}$  and photo-generated carrier density  $\Delta n$ :

$$V_{oc} = \left(\frac{kT}{q}\right) \ln \left[ \frac{\Delta n(N_A + \Delta n)}{n_i^2} + 1 \right] \quad (8)$$

## 2.2 Thin Film Solar Cell Structure

Thin film solar cells achieve light to electricity conversion with cell structures on the order of several microns thick. This is accomplished by utilizing an absorber layer made of a direct band gap semiconductor with a high absorption coefficient. Thin film solar cells typically utilize a sandwich structure of layers as illustrated in Fig. 2.4. Most thin

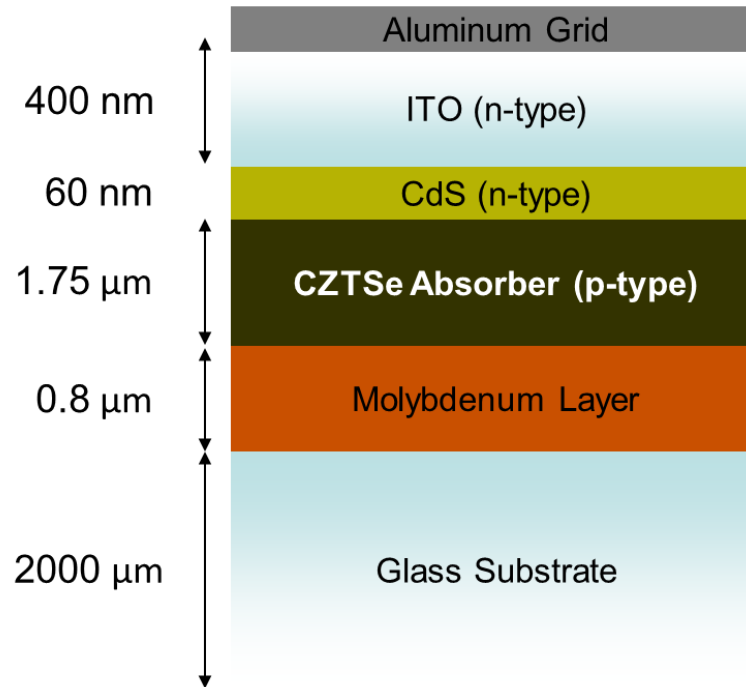


**Figure 2.4:** Cross-sectional view of typical thin film solar cell structure with CZTSe absorber layer

film solar cells utilize a p-n heterojunction formed by a p-type absorber and an n-type emitter of different band gaps. The n-type emitter typically consists of a thin layer of wide band gap semiconductor such as CdS to form the p-n junction and a degenerately doped n-type transparent conductive oxide (TCO) to increase shunt resistance and to provide a transparent top electrode.

A material must exhibit particular optical absorption properties in order to qualify as a thin film solar cell absorber layer. The band gap is a key property that has a strong impact on the quality of optical absorption as well as the ultimate performance the device can achieve. The energy of the band gap puts a lower limit on the photon energy that can be absorbed as it represents the minimum energy difference between the top of the valence band and the bottom of the conduction band. In addition, if the top of the valence band

and the bottom of the conduction band are not at the same value of electron momentum, then direct transitions from the valence band to the conduction band are not allowed. This situation is referred to as an indirect band gap and electrons must undergo an additional interaction with a lattice vibration or a phonon in order to obtain enough momentum to transition to the conduction band and generate an electron-hole pair. This extra interaction occurs at a much slower rate and makes indirect band gap semiconductors, such as silicon, weaker absorbers compared to direct band gap semiconductors particularly at energies near the band gap.

The band gap of the absorber layer also puts a limit on the theoretical maximum efficiency of a solar cell in which it is utilized. Figure 2.5 shows how the maximum theoretical efficiency of a single junction solar cell relates to absorber layer band gap as calculated by William Shockley and Hans Queisser in 1961[11]. It can be seen that the optimal band gap is approximately between 1.2 and 1.4 eV where the theoretical efficiency reaches 33.7% for 1.34 eV. The Shockley-Queisser efficiency limit has served as a basis for determining ideal candidates as absorber layers in thin film solar cells.

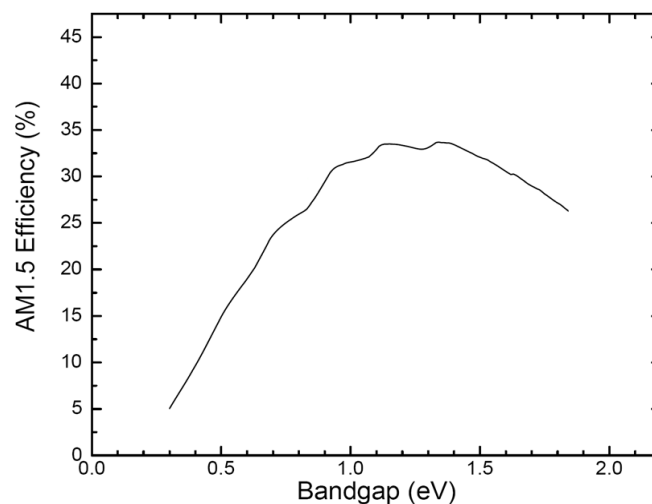


**Figure 2.5:** Shockly-Quiesser limit on theoretical efficiency with respect to absorber layer band gap

### 2.3 CZTSe Absorber Layer

$\text{Cu}_2\text{ZnSnSe}_4$  (CZTSe) is the pure selenide form of the  $\text{Cu}_2\text{ZnSn}(\text{S}_x\text{Se}_{1-x})$  (CZTSSe) quaternary compound. CZTSSe is an extension of the sulfide mineral  $\text{Cu}_2(\text{Zn,Fe})\text{SnS}_4$  known as kesterite which was first reported after a mineral find in 1958 and  $\text{Cu}_2\text{ZnSnS}_4$  (CZTS) was synthesized soon after in 1960 [12]. The kesterite crystal structure can be described as an adamantine structure with tetrahedral bonding where each metal ion (cation) is bonded with four chalcogen atoms (anions). The application of CZTSSe as a thin film photovoltaic absorber layer evolved from the success in device performance achieved by its chalcopyrite predecessor  $\text{Cu}_2\text{InGaSe}_2$  (CIGS). The kesterite showed potential as a low-cost substitute for CIGS due to the similarities in crystal structure and optoelectronic properties. The kesterite structure can be derived from the CIGS chalcopyrite structure by substituting Zn and Sn for In/Ga as can be seen in Fig. 2.6.

CZTSSe is a mixture of the pure sulfide CZTS and pure selenide CZTSe and has been shown to have a tunable band gap by varying S/Se composition ratio. The band gap can

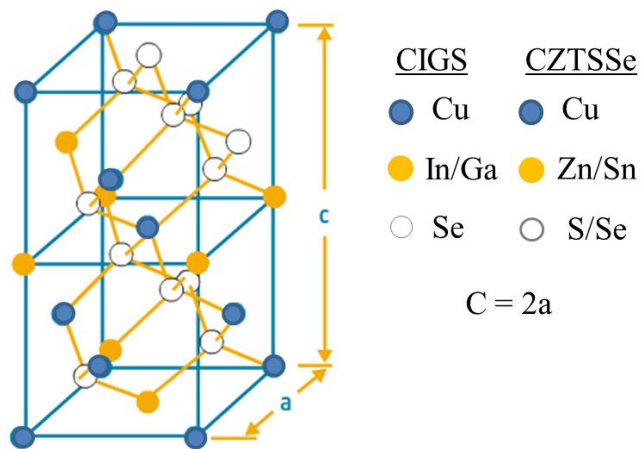


**Figure 2.6:** Crystal structure for both CIGS and CZTSSe with cation substitution

be tuned across the optimal range of the Shockley-Queisser limit with CZTSe having a band gap of 1.0 eV and CZTS has a band gap of 1.5 eV. This gives CZTSSe versatility in achieving an ideal band gap and matching to different n-type emitters to reduce band offset at the p-n heterojunction. In CZTSSe cell structures, the materials typically chosen for the n-type emitter layer have a wide band gaps ( $> 2.0$  eV) to allow sun light to transmit through to the absorber layer. This can result in a conduction band offset that will lead to large interface recombination [13]. Despite the fact that 1.34 eV is the optimal band gap, thin film solar cells utilizing a CdS/CZTSSe junction have achieved the best performance with band gaps closer to 1.1 eV. The current cell record efficiency of 12.6% was obtained with a  $\text{Cu}_2\text{ZnSnS}_{0.3}\text{Se}_{0.7}$  absorber layer with a band gap of 1.13 eV and CZTSe continues to outperform CZTS.

#### 2.4 CZTSe Fabrication: Sputtering

Many methods of thin film deposition and growth have been utilized in CZTSe fabrication with physical vapor deposition (PVD) being one of the most practical for industry scale production. Sputtering is a form of PVD by which materials are removed from a target by the bombardment of energetic particles and deposited on a substrate. The sputtering process is carried out in a vacuum chamber that is first pumped down to high vacuum and then back filled with an inert gas such as argon(Ar). A large, negative bias is applied to the target and an electric field is produced which accelerates electrons into ionizing collisions with the Ar atoms generating a plasma of  $\text{Ar}^+$  ions. These ions are accelerated toward the target by the electric field and gain sufficient energy to dislodge material upon collision. In the case of targets consisting of a nonconducting material, an

AC power signal is required to prevent the target from charging and repelling the  $\text{Ar}^+$  ions which would stop the sputter process. This is known as radio frequency (RF) sputtering because the frequency must be in the range of radio waves in order to prevent repulsion of the  $\text{Ar}^+$  ions during positive cycles of the power signal.

Sputtering offers the advantage of uniform large area deposition with precise control of deposition rate and film structure. These parameters can be fine-tuned by adjusting the power applied to the target, Ar pressure, and flow rate. For compound materials, multiple targets can be employed simultaneously in a process called co-sputtering. Figure 2.7 is a schematic of a typical co-sputtering arrangement utilizing three targets. The confocal point of three targets is centered on the substrate which is rotated to produce a uniform film. The deposition rate of each target can be precisely controlled to produce a film with a desired stoichiometry. The control of deposition rate and high degree of film uniformity offered by co-sputtering makes it a useful method for CZTSe fabrication because it has been demonstrated that stoichiometry has a large impact on grain growth and device performance [14].

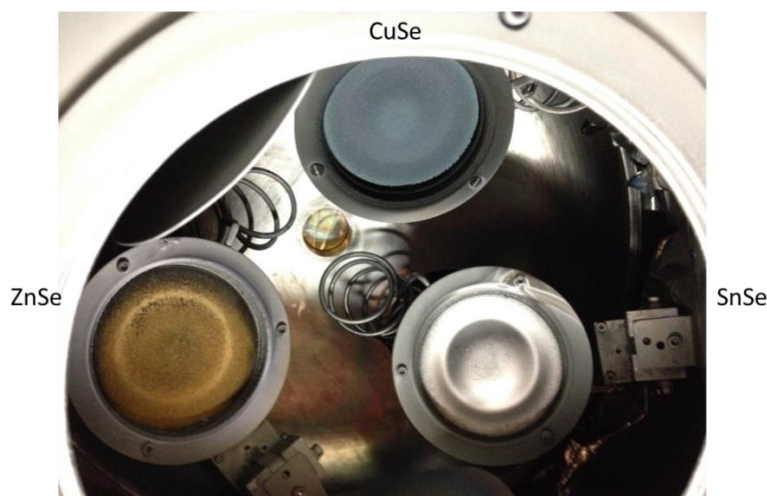
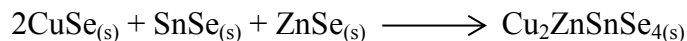


**Figure 2.7:** Image of co-sputter target configuration used in this study

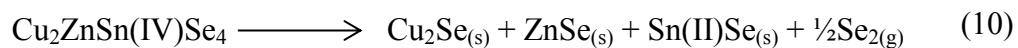
## 2.5 CZTSe Fabrication: Annealing

Following precursor deposition, a high-temperature annealing process must be carried out to form the CZTSe film. Research on the formation of  $\text{Cu}_2\text{ZnSnS}_4$  (CZTS) has produced valuable insights into the reaction kinetics and precursor phase stability during the annealing process. These insights are extended to CZTSe and applied to the following formation reaction: (9)



The temperature range required to optimally initiate this reaction has been found to be between 550–600 °C. At these temperatures, the volatility of the binary chalcogens must be considered and suppressed in order to prevent film decomposition. It has been shown that Sn in CZTSe is in a +IV oxidation state and Sn(IV) is stable as  $\text{Sn(IV)Se}_2$ .

Experiments on S and Sn loss during annealing of CZTS showed that Sn becomes volatile when reduced from the Sn(IV) to the Sn(II) oxidation state [15]. This reduction in oxidation state forms Sn(II)Se secondary phase which displaces the equilibrium of the reaction and leads to the following decomposition paths:



In order to prevent Sn(IV) from undergoing a reduction reaction to Sn(II), an oxidizing environment of  $\text{Se}_{2(g)}$  can be supplied to the system. The  $\text{Se}_2$  vapor environment will oxidize Sn(II)Se to form  $\text{Sn(IV)Se}_2$  and will remain stable given a proper level of  $\text{Se}_2$  vapor pressure is maintained while the sample is annealing.

The amount of  $\text{Se}_2$  vapor pressure required to stabilize each binary reactant can be determined by the Gibbs free energy of formation which relates the favorability of



precursor decomposition to  $Se_2$  partial pressure and temperature by:

$$\Delta G = 2.303RT \log \left( \frac{P_{Se_2}}{P_0} \right) \quad (12)$$

where R is the molar gas constant, T is temperature,  $P_{Se_2}$  is the partial pressure of selenium and  $P_0$  is the standard pressure of  $10^5$  Pa. The experimental literature values for the Gibbs free energy of formation for each binary reactant are listed in Table 2.1. Each line in Fig. 2.8 represents the minimum  $P_{Se_2}$  required for each binary reactant to retain stability at a given temperature. It can be seen that  $Sn(IV)Se_2$  requires  $P_{Se} = 2$  Pa in order to remain stable at an annealing temperature of  $580$  °C. The black line in Fig. 2.8 is a plot of Se vapor pressure which is sufficient to stabilize all reaction species across the range of annealing temperatures [16].

**Table 2.1:** Literature values for the Gibbs free energy of relevant reactions [17]

Reaction	Temperature Range (K)	$\Delta G$ (kJ/mol)
$4Cu^0 + Se_2 \leftrightarrow 2Cu_2^I Se_2$	398-1358	$0.060T - 244$
$2Cu_2^I Se + Se_2 \leftrightarrow 4Cu^{II} Se$	4 -398	$0.183T - 171$
$2Sn^0 + Se_2 \leftrightarrow 2Sn^{II} Se$	505 -700	$0.187T - 135$
	700 – 813	$0.182T - 321$
$2Sn^{II} Se + Se_2 \leftrightarrow 2 Sn^{IV} Se_2$	4 – 813	$0.168T - 310$
$2Zn^0 + Se_2 \leftrightarrow 2Zn^{II} Se$	4 – 613	$0.204T - 207$
	298 -613	$0.167T - 476$

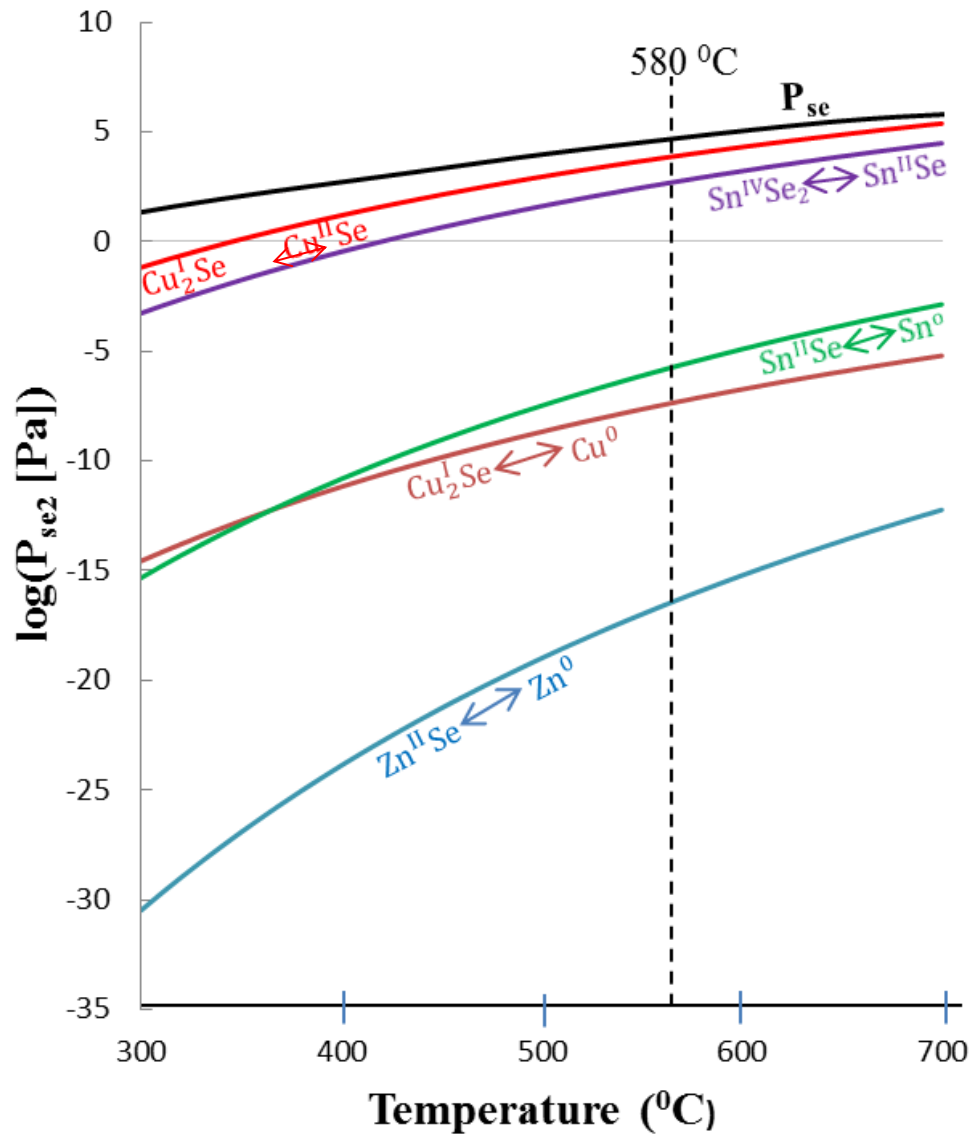


**Figure 2.8:** Plot of  $P_{\text{Se}_2}$  vs T for each binary chalcogen precursor oxidation state transition. At an annealing temperature of 580 °C, a vapor pressure of 2 Pa is required to stabilize  $\text{Sn}^{\text{IV}}\text{Se}_2$

## 2.6 Incorporation of Sodium

The incorporation of Na during the synthesis of CIGS has proven useful for supplementing the fabrication process and producing devices with optimal performance [18]. The Na introduced into the CIGS system has been shown to behave as a fluxing agent to promote large grain growth with grain boundary passivation. It has been suggested that Na forms a liquid solution of  $\text{Na}_2\text{Se}_x$  which accumulates at grain boundaries and provides a surfactant effect enhancing grain growth, thereby improving electronic properties [19]. The effects of Na are important to understand because soda lime glass (SLG) which contains about 13wt% Na is an ideal substrate for thin film PV due to low cost and appropriate thermal expansion coefficient [20]. Many different Na incorporation methods have been researched to determine the optimum concentration to be incorporated into the manufacturing process. It has been determined that depositing 20 nm thick layer Na on top of the molybdenum(Mo) back contact prior to precursor deposition was the optimum incorporation method for CIGS manufacturing. This provided a uniform distribution of Na into the system and Mo targets are now made pre-doped with Na for the manufacturing of CIGS solar cells [21].

Research on Na incorporation in CZTSe has shown to have similar beneficial results [22]. However, most of the research has been conducted on pure sulfides with little data on the effects of pure selenides. Furthermore, there is still a lack of consensus in the literature on the optimal Na precursor thickness for CZTSe fabrication. For this reason Na incorporation is still a necessary topic of research that could further increase the quality of the CZTSe fabrication process.

## 2.7 Combinatorial Analysis

A combinatorial analysis is commonly used in thin film fabrication in order to study the local effects of variations in film composition. Combinatorial experiments offer the advantage of creating a single sample that represents a wide range of stoichiometry as depicted in Fig. 2.9. A combinatorial deposition is achieved by performing a non-uniform deposition of the elemental constituents across a substrate. Using a robotically controlled deposition mask is a common and effective way of producing a sample with a desired composition profile. Performing a combinatorial deposition of Na with CZTSe could provide information on the optimal thickness of Na to be supplied prior to precursor deposition and provide insight into the transport mechanisms of Na through CZTSe during annealing.

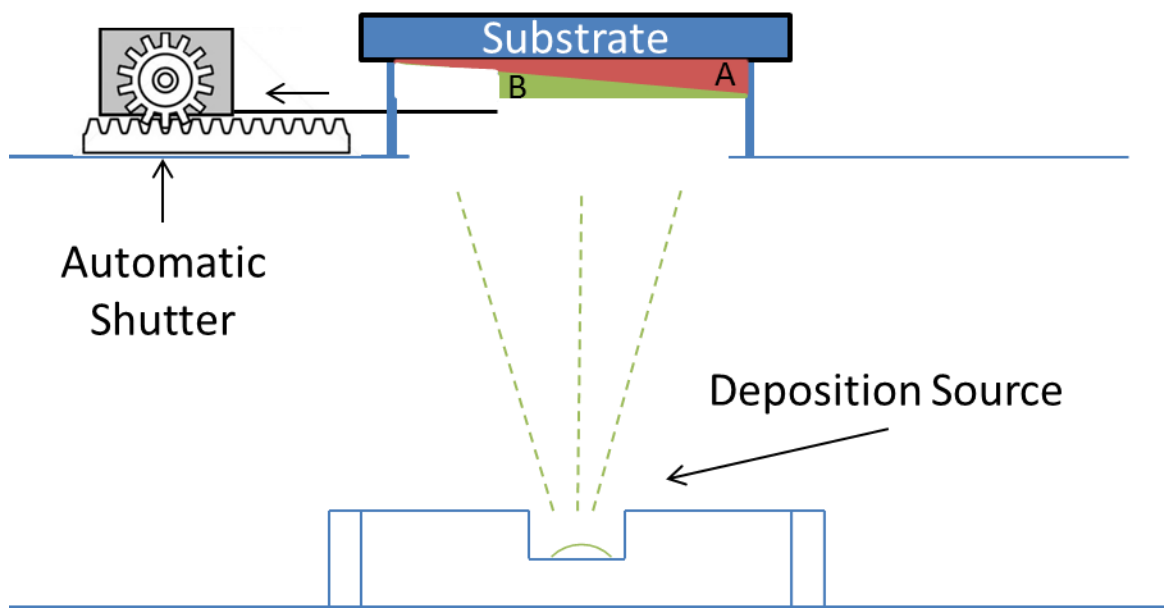


**Figure 2.9:** Illustration of a combinatorial deposition using a robotically controlled shutter. Films A and B are deposited with a linear thickness gradient to give a full range of composition across substrate

## CHAPTER 3

### EXPERIMENTAL PROCEDURES

#### 3.1 CZTSe Thin Film Fabrication

$\text{Cu}_2\text{ZnSnSe}_4$  (CZTSe) thin films were prepared by RF co-sputtering from three binary selenide targets, CuSe, ZnSe, SnSe, and then annealed at  $580^\circ\text{C}$  for 20 minutes. In order to control Na and K incorporation, alkali free Corning Eagle glass was chosen as the substrate. The Eagles glass was cut into 3" x 3" substrates and then cleaned with a 10 minute isopropyl alcohol scrub, followed by 15 minutes in a Liquinox solution held at  $60^\circ\text{C}$  in an ultrasonic bath and 10 minutes in an automated spin rinse/drier. The substrates were then sputter coated with  $\sim 800$  nm molybdenum (Mo) at UHV Sputtering INC. A Mo thickness of 800 nm is sufficient to act as diffusion barrier to keep any residual Na, K and any other contaminants from diffusing from the substrate into the CZTSe, as well as provide optimum conductivity. The sputtering procedure consisted of 2 minutes at a working pressure of 2 mTorr to optimize adhesion followed by 60 minutes at a working pressure of 10 mTorr to optimize conductivity.

Precursor films were deposited by a RF co-sputtering system equipped with three 75 mm diameter targets, a deposition controller,  $\text{LN}_2$  cooled tubing for cryosurface pumping, a turbo-molecular pump backed by a mechanical roughing pump, a geared motor for sample rotation and a chiller for circulating  $18^\circ\text{C}$  de-ionized (DI) water through the

targets and turbo pump to prevent overheating. After loading the Mo coated substrates, the chamber was pumped down to a base vacuum of  $8 \times 10^{-7}$  Torr and then back filled with argon to a working pressure of 10 mTorr at a flow rate of 20 sccm. Power was then supplied to the targets at values calibrated to deposit stoichiometric amounts of CuSe, ZnSe, and SnSe in optimal time. The sputtering rates vs. power for each target are plotted in Fig. 3.1. Due to the difference in deposition rate vs. power and heat transfer characteristics of each target, the sputter recipe had to be optimized within certain constraints. The sputtering rate for ZnSe was much lower than the other two targets so the recipe was tailored around maximizing the ZnSe sputtering rate. In addition, if the CuSe target exceeded 110 W, the target temperature would exceed the melting temperature of the indium bonding on the copper backing plate, resulting in a short.

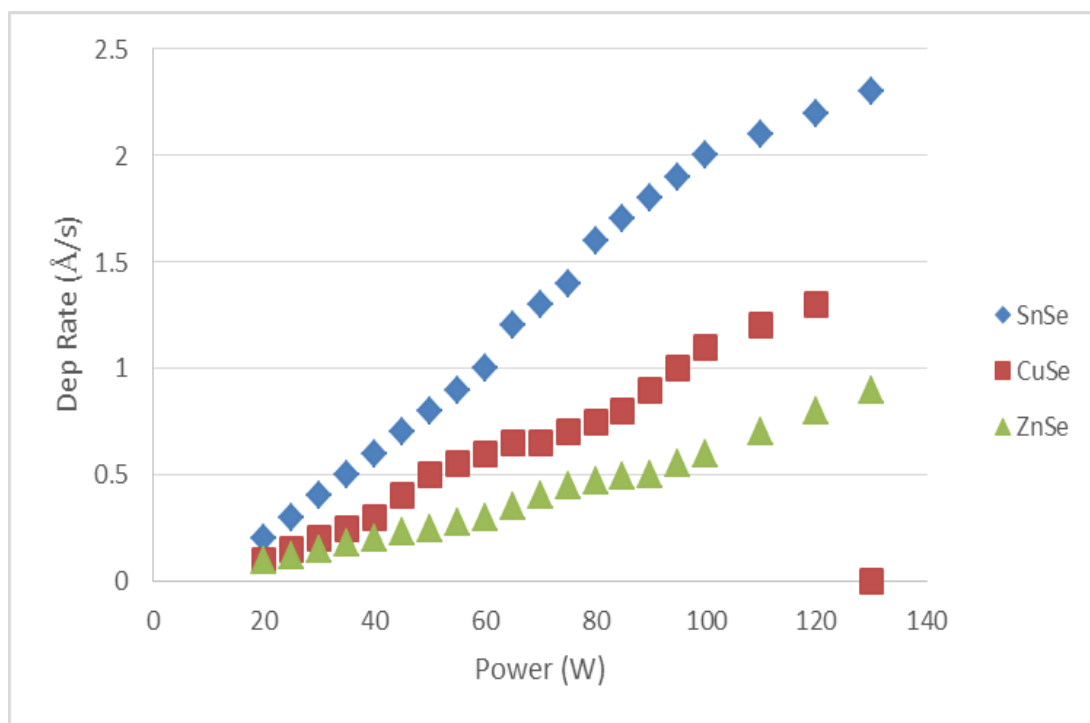


**Figure 3.1:** Deposition rate vs. power trends for the three binary selenide targets

The optimal power levels for each target were determined to be 77 W for ZnSe, 72 W for CuSe, and 45 W for SnSe. The deposition was carried out for 1 hr and 15 min which resulted in a film with a thickness  $\sim 1.0 \mu\text{m}$ . The uniformity of the deposition was determined using a Kapton tape mask to form steps in the film along the edges and from the center of the film out to an edge. Despite substrate rotation and careful alignment of the confocal point to the center of the substrate holder, thickness measurements of the steps using a Tencor P-10 profilometer determined a thickness reduction at the center edges of  $\sim 0.5\%$  and  $\sim 2\%$  at the corners. Due to the decreased uniformity in thickness at the corners, the  $3 \times 3 \text{ in}^2$  substrates were reduced to  $3 \text{ in} \times 1 \text{ in}$  strips before precursor deposition.

Annealing was carried out in a custom built vacuum chamber that contained a 6 inch diameter substrate heater controlled with a Eurotherm programmable process controller. In order to supply a high Se vapor pressure above the sample during annealing, a box machined out of graphite was made and is imaged in Fig 3.2. The graphite box consisted of a center area to accommodate a substrate up to  $3 \times 3 \text{ in}^2$ , an outer recess to contain selenium pellets, and a slot drilled in the base where a thermocouple was inserted. The thermocouple slot was drilled such that the thermocouple sat approximately 1-2 mm directly under the substrate to minimize temperature offset. The lid and the base of the graphite box formed a good seal that effectively contained Se vapor in the small volume directly above the substrate. However, the seal was not perfect and a small amount Se vapor would leak out during the annealing process and coat the walls of the chamber. In addition, the porosity of the graphite absorbed the Se vapor in the box where it would condense and evaporate again in future annealing cycles. These two factors made



**Figure 3.2:** Graphite box base containing 3x3 in<sup>2</sup> substrate surrounded by a recess where selenium pellets are placed

controlling the concentration of Se in the box difficult so indiscriminate amounts of Se was supplied to the graphite box every annealing cycle to assure the presence of Se throughout the entire cycle.

After the sample was prepared in the graphite box and loaded into the chamber, annealing procedure began by first performing a purging cycle using a mechanical roughing pump and ultra-high purity nitrogen (N<sub>2</sub>). The chamber was then filled to 1 atm of N<sub>2</sub> and the substrate heater was ramped up at 30 °C/min to 580 °C where annealing commenced for 20 min. The chamber was then allowed to cool naturally back down to room temperature.

### 3.2 NaF Thickness Gradient Deposition

A NaF thickness gradient was deposited by thermal evaporation from a tungsten boat with an automatic, programmable, constant withdrawal shutter placed beneath the



substrate. The thermal evaporator was built in lab and consisted of a steel bell jar, a Variac controlled step down transformer, and a diffusion pump backed by a mechanical roughing pump which provided an ultimate vacuum of  $3 \times 10^{-5}$  Torr. The automatic shutter, imaged in Fig. 3.3, consisted of a Teflon gear powered by a servo motor fixed to a steel plate which rolled on a linear gear track also made out of Teflon. Teflon is one of the very few plastics that can be incorporated in a vacuum system due to its low outgassing rates [23]. The servo was connected to an external control circuit via an electrical feedthrough flange which was interfaced with an Arduino Uno to program the shutter to withdraw at a desired constant rate. Deposition would begin with the shutter closed and when a desired deposition rate was reached and stabilized the shutter would be programmed to withdraw over the length of the substrate for the time required to deposit the desired thickness of the high side of the gradient.

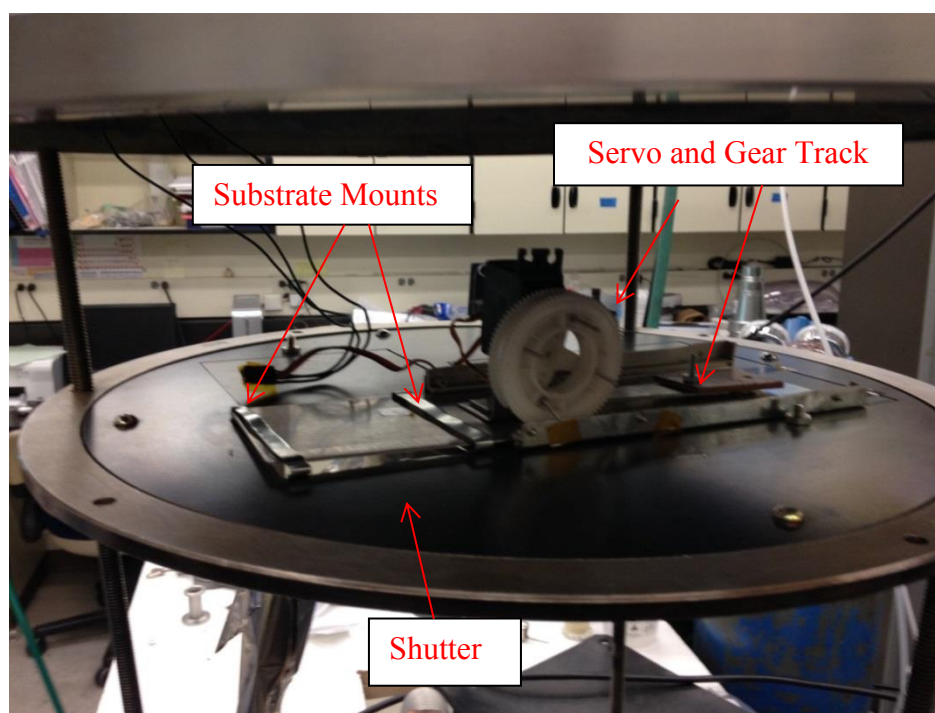


**Figure 3.3:** Image of automatic constant withdrawal shutter used to deposit NaF thickness gradient for combinatorial analysis (evaporation source below not imaged)

The NaF gradient was deposited on the 3 in x 1 in Mo coated substrates as described above. The substrate holder was designed to mask two long regions on both ends of the substrate from the NaF deposition which can be seen in Fig. 3.4. This resulted in a substrate with a 50 mm long NaF gradient with two 14 mm uncoated regions to provide an un-doped reference. To measure the linearity of the thickness gradient, a deposition was performed with Kapton tape applied to mask off a region along the NaF gradient. A thickness measurement was made every 3 mm along the film gradient using a Tencor profilometer. Roughness of the substrate, the NaF film, as well as imperfections in the step introduced errors in the measurements, especially in the thinner region of the film, but a linear trend can be resolved as depicted in Fig. 3.5. The film was then sent through the CZTSe fabrication process described above.



Figure 3.4: NaF film with thickness gradient prior to loading into sputtering chamber for CuSe-ZnSe-SnSe deposition.

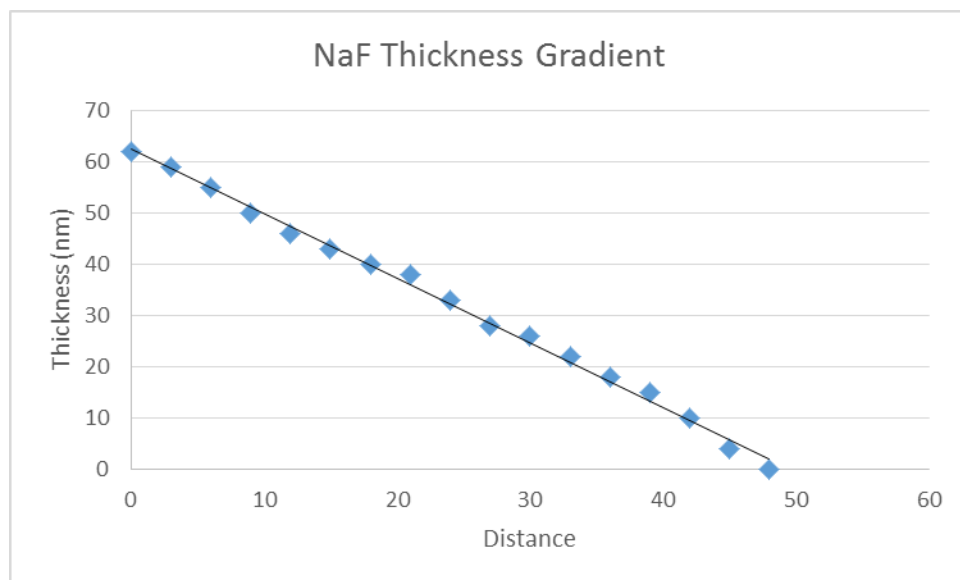


Figure 3.5: Thickness measurements taken along the length of the gradient. Slope of line shows an approximate reduction in thickness of 1.3 nm/mm across substrate

## CHAPTER 4

### RESULTS AND DISCUSSION

#### 4.1 Energy-dispersive X-ray Spectrometry Calibration

Energy-dispersive X-ray Spectrometry (EDS) is a method for rapid, nondestructive elemental composition analysis and is utilized in this study for all thin film stoichiometry determination. Measuring elemental composition using EDS is achieved by detecting the emission of X-rays produced by bombarding a sample with a focused, high energy beam of electrons. The interaction between a beam electron and an atom within the sample results in the ejection of an inner shell electron and creates a hole which is subsequently filled by the relaxation of an outer shell electron. This relaxation emits an X-ray with energy equal to the difference of the outer and inner electron shell which is characteristic to the type of atom from which the X-ray originates.

Performing a quantitative elemental analysis using EDS involves correlating the intensity of a measured X-ray spectral line with the relative amount of the corresponding element within the sample. In order to obtain an accurate analysis, the results must be calibrated using a standard sample of known composition to account for any systematic errors. In this study, a CZTSe standard was obtained by applying a technique called Rutherford Backscattering Spectrometry (RBS) on a sample fabricated using the process described in Chapter 3. RBS determines the elemental composition of a material

by scattering ions from nuclei within the material. This technique produces an accurate quantitative elemental analysis without the need of a standard. The results of the RBS analysis are shown in Table 4.1 along with EDS results of the standard obtained from two scanning electron microscopes with EDS capabilities. The results show a difference between the two instruments with the Quanta having less error compared to the Hitachi. This suggests that there is a large amount of instrument induced error with the Hitachi so all EDS analysis performed in this study was done with the FEI Quanta 600F.

#### 4.2 Chemical and Structural Results

The fabrication process was successful at maintaining film stability during annealing and producing near stoichiometric films as measured by Energy-dispersive X-ray Spectroscopy (EDS). However surface imaging with a scanning electron microscope (SEM) revealed blister formation up to 50  $\mu\text{m}$  in diameter in high density. These blisters appeared to be trapped gas within the film which resulted in film delamination upon rupture. This was validated by EDS elemental composition measurements on intact and ruptured blister which are contained in Fig. 4.1. The EDS measurements reveal that the intact blisters maintain the same composition as the adjacent film whereas the ruptured blisters only contain molybdenum and selenium. Blister formation of this nature is well

Element	RBS At%	FEI Quanta 600F	%Error	Hitachi S-3000N At%	%Error
Sn	10	9	10	8	20
Cu	17	14	17	12	29
Zn	13	11	15	20	54
Se	60	66	10	60	0

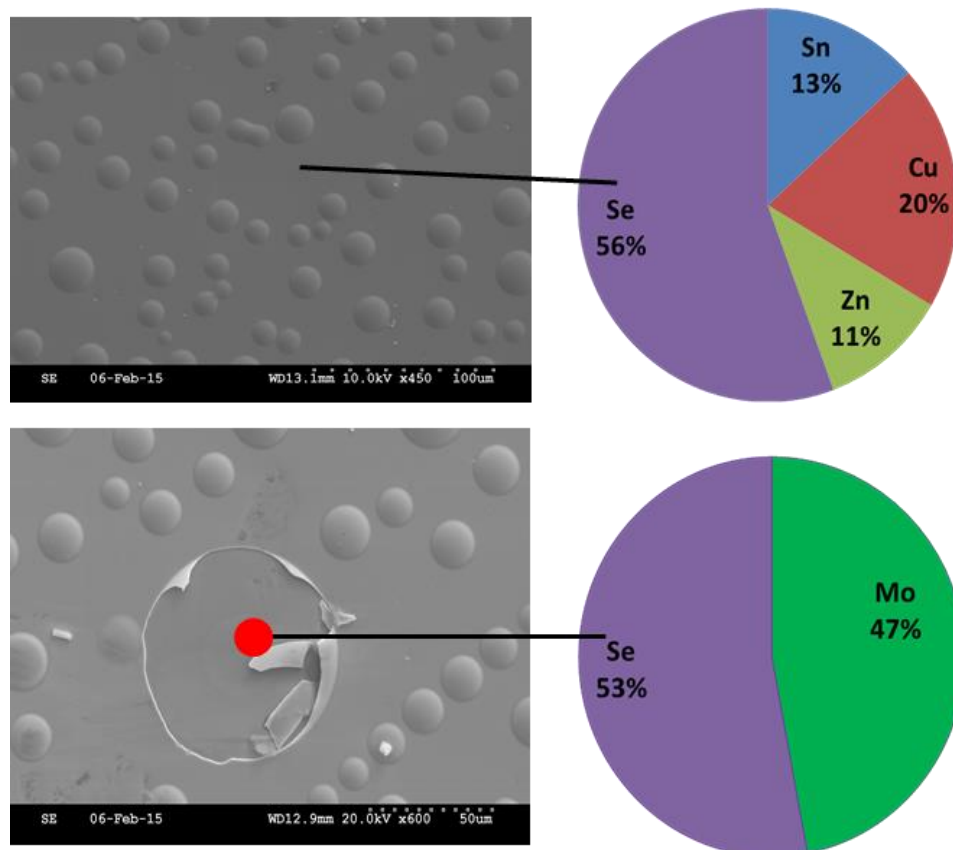


**Figure 4.1:** SEM images of blisters with corresponding EDS results caused trapped Ar during sputtering

documented in the literature as Ar gas entrapment that develops during sputtering which migrates and nucleates during annealing [24]. It has been shown that the density of the blister formation is dependent on sputter pressure. For this reason, the sputter pressure was reduced from 10 mTorr to 6.8 mTorr which reduced blister formation to not at all or very seldom occurrences.

After readjusting the sputter recipe for the new working pressure, the fabrication method continued producing near stoichiometric CZTSe thin films though slightly selenium rich. The image of the surface in Fig. 4.2 reveals that the film consists of nano-

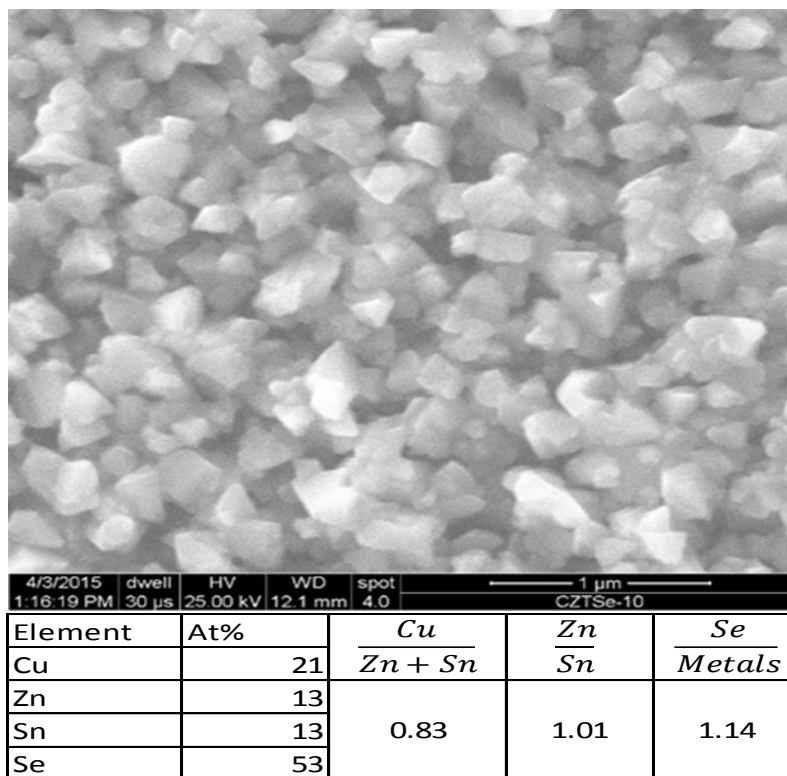


**Figure 4.2:** SEM and EDS results of fabricated CZTSe thin film

crystalline grains roughly 300 – 400 nm in size. The image also shows the formation of voids indicating the surface was on the verge of volatilizing. The existence of small grains and surface voids are an indication that the annealing process was not sufficient enough to further grow grains once the CZTSe phase was formed. However, the EDS results show the film contains excess selenium which indicates that the film maintained its selenium content which possibly diffused through the precursor film to the back contact forming  $MoSe_2$ . The surface grains of the film displayed good uniformity across the surface area of the film with no secondary phase segregation.

To study phase formation within the film X-ray diffraction (XRD), data were recorded using a Phillips X'Pert X-ray diffractometer with  $CuK_{\alpha 1}$  radiation. The XRD pattern for the film shown in Fig. 4.3 contains the three highest intensity peaks consistent with

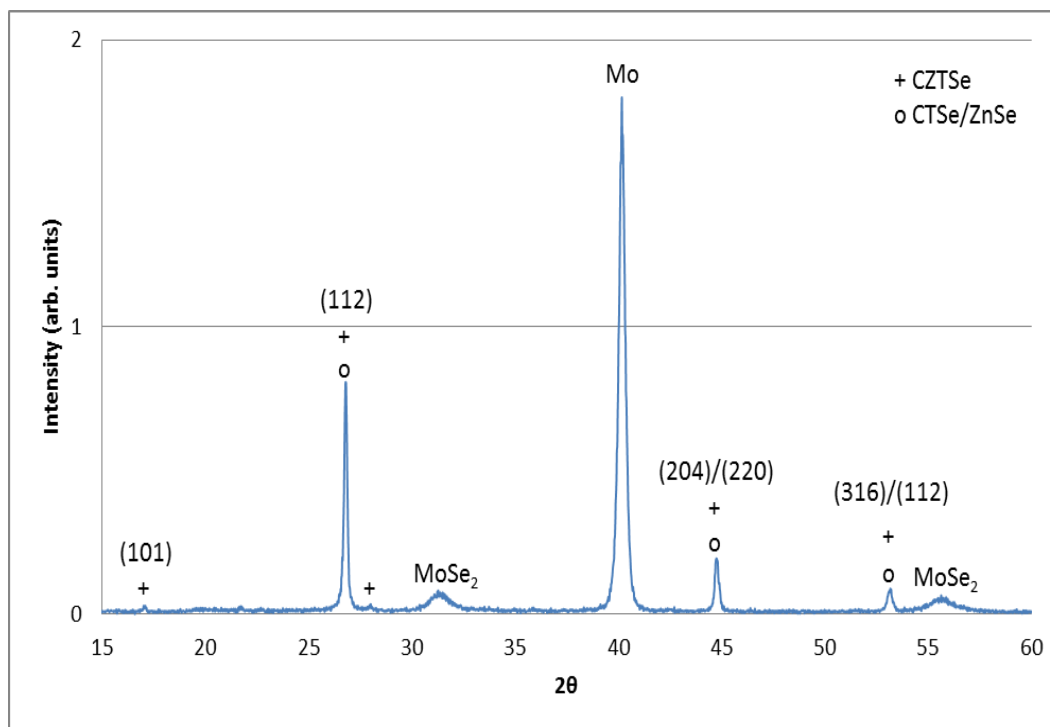


**Figure 4.3:** X-ray diffraction pattern of CZTSe film showing only minor MoSe<sub>2</sub> secondary phase formation

tetragonal CZTSe with the exception of the Mo peak at 40°. The peaks at 27.1°, 45°, and 53.5° correspond to the (112), (204), and (312) planes of the CZTSe unit cell, respectively, and are consistent with the Cu<sub>2</sub>ZnSnSe<sub>4</sub> crystallographic reference data (PDF54-868). There are no detectible peaks corresponding to the precursor binary selenides, indicating the annealing recipe was effective at carrying the reaction toward the formation of CZTSe. However, the lattice constants for ZnSe and CTSe are nearly identical to CZTSe, making the detection of these secondary phases nearly impossible by XRD peak matching. The two short and broad peaks at 31.35° and 55.7° match up best with the reference data on MoSe<sub>2</sub> (PDF17-887).

In order to evaluate the crystallite size, which is typically similar to the grain size of

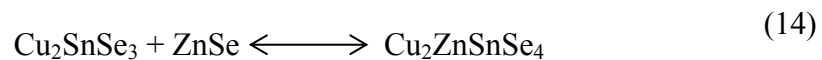


thin films, the Scherrer equation was applied. This equation describes the relationship between peak broadening ( $\beta$ ), in this case the full width at half max (FWHM), and average crystallite size ( $L$ ) with the following formula:

$$L = \frac{K\lambda}{\beta \cos(\theta)} \quad (13)$$

where  $\lambda$  is the X-ray wavelength used (0.154060 nm),  $\theta$  corresponds to the  $2\theta$  position of the peak, and  $K$  is the shape factor taken to be 0.9 for approximately spherical crystallites. The  $\beta$  in this equation is expressed in radians and has been corrected to eliminate instrument-induced peak broadening using the 640d silicon powder line shape standard from the National Institute of Standards and Technology. Applying the Scherrer relation to the  $\text{MoSe}_2$  peaks gives  $L = 12.27$  nm which could correspond to the thickness of  $\text{MoSe}_2$  grains.

The Raman spectrum of the sample is contained in Fig. 4.4 which was obtained using a  $\lambda = 488$  nm laser and calibrated using a monocrystalline Si standard. The spectrum displays prominent peaks at frequency shifts corresponding to  $139 \text{ cm}^{-1}$  and  $233 \text{ cm}^{-1}$  which are consistent with the  $\text{Cu}_2\text{ZnSnSe}_4$  phase. However, the broadness of the spectrum out to  $155 \text{ cm}^{-1}$  and  $260 \text{ cm}^{-1}$  could be due to the convolution of peaks corresponding to  $\text{ZnSe}$  ( $250 \text{ cm}^{-1}$ ) and  $\text{CTSe}$  ( $180 \text{ cm}^{-1}$ ) phases. The existence of these phases suggest that the annealing process was either unsuccessful at bringing the CZTSe formation reaction to completion or the sample may have over annealed resulting in the CZTSe to slightly decompose following this reaction:



In order to examine the optical properties of the film, a second film was fabricated on

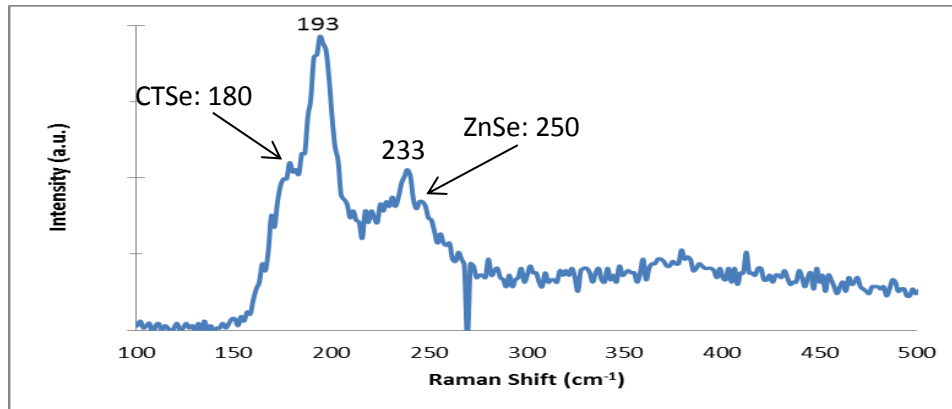


**Figure 4.4:** Raman spectra data detecting the major peaks of CZTSe at  $193\text{ cm}^{-1}$  and  $233\text{ cm}^{-1}$

a glass substrate without the Mo coating using the same fabrication recipe. The Mo coating would block light transmission through the CZTSe film, making accurate measurements difficult. The optical absorption properties of the film were analyzed using UV-Vis-NIR spectroscopy and plotted in Fig 4.5. The absorption coefficient ( $\alpha$ ) can be calculated from the transmission (T), reflection (R), and film thickness (d) by rearranging Beer's Law:

$$\alpha(\text{cm}^{-1}) = -\frac{1}{d(\text{cm})} \ln\left(\frac{T}{(1-R)^2}\right) \quad (15)$$

The absorption coefficient  $\alpha$  calculated in equation (2) can be used to determine the band gap  $E_g$  by generating a plot from the following relation:

$$(\alpha)^{1/p} = h\nu - E_g \quad (16)$$

This equation states that at photon energies above  $E_g$ ,  $(\alpha)^{1/p}$  will increase linearly with  $h\nu$  and  $E_g$  will be approximately equal to the photon energy for  $\alpha = 0$ . The p in equation (16) is a transition-dependent exponent and is equal to  $\frac{1}{2}$  for direct band gap transitions 2 for indirect. Since CZTSe has been shown to be a direct band gap semiconductor, p is set to  $\frac{1}{2}$  and the relation is plotted in Fig. 4.6.

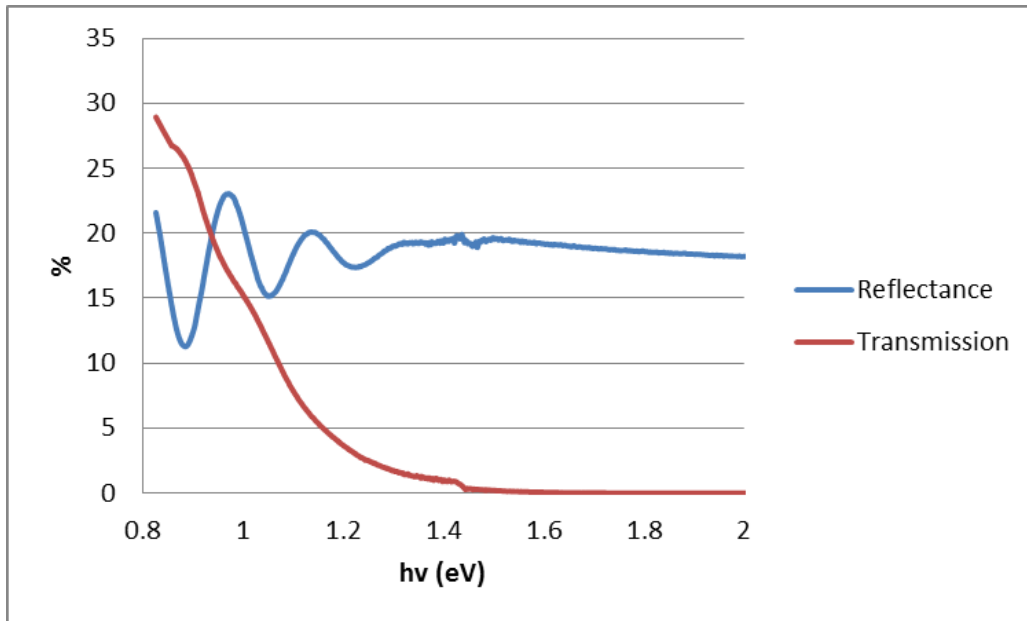


**Figure 4.5:** Optical characteristics of CZTSe film used for band gap and absorption coefficient calculation. %Transmission and Reflectance

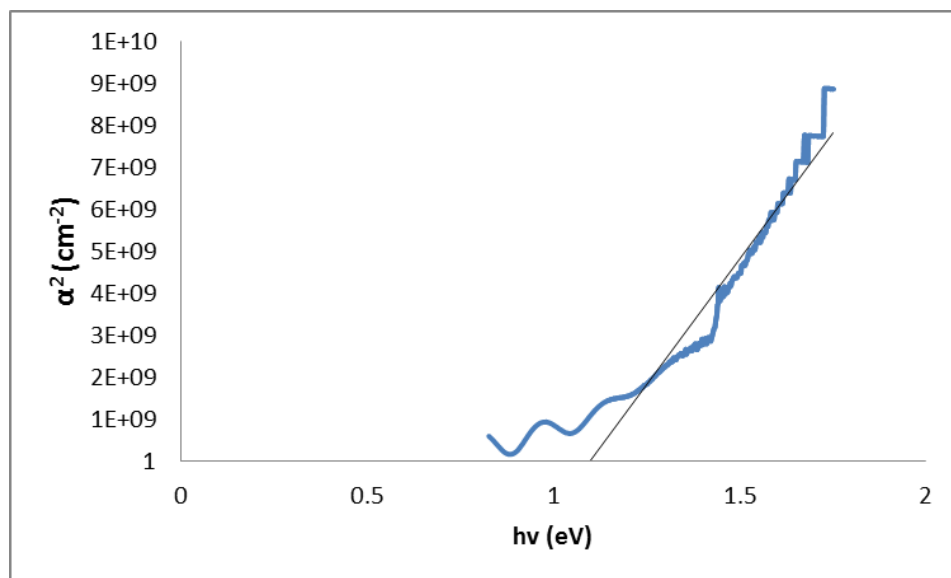


**Figure 4.6:** Absorption coefficient and Tauc plot showing band gap estimation

The transmission data in Fig. 4.5 shows that the film is optically transparent for photon energies up to 1.2 eV and then the film becomes highly absorbent. The plot of absorption coefficient in Figure 4.6 shows an absorption coefficient  $\alpha > 10^4 \text{ cm}^{-1}$  and extending the linear regression to the energy axis in yields an  $E_g$  between 1.0 eV and 1.1 eV. The dip around 1.45 eV is due to noise from detector change in the monochromator so the band gap is most likely closer to 1.0 eV.

### 4.3 NaF Doping Analysis: Delamination

First attempts at fabricating CZTSe thin films with a NaF thickness gradient resulted in severe film delamination. Films fabricated without NaF all exhibited good adhesion so the delamination was attributed to the incorporation of the underlying NaF layer. It was found that the tendency for film delamination increased with film thickness and thicknesses greater than  $\sim 40 \text{ nm}$  would immediately delaminate upon exposure to the air after sputtering. Films with NaF thicknesses less than 40 nm were stable in the air but would periodically delaminate during annealing.

This delamination issue has been attributed to the hygroscopic nature of NaF. Hygroscopy is a measure of a materials ability to absorb water from the surrounding environment such as the humidity in the air. As the NaF absorbs water vapor from the air, the  $\text{H}_2\text{O}$  molecules become suspended within the NaF structure, resulting in a large volume expansion which over-stresses the film and results in delamination. To demonstrate the high degree of sensitivity to moisture of precursor films due to NaF incorporation, a single drop of de-ionized water was pipetted onto a film that contained a region with NaF and without. The image of the result in Fig. 4.7 clearly shows the

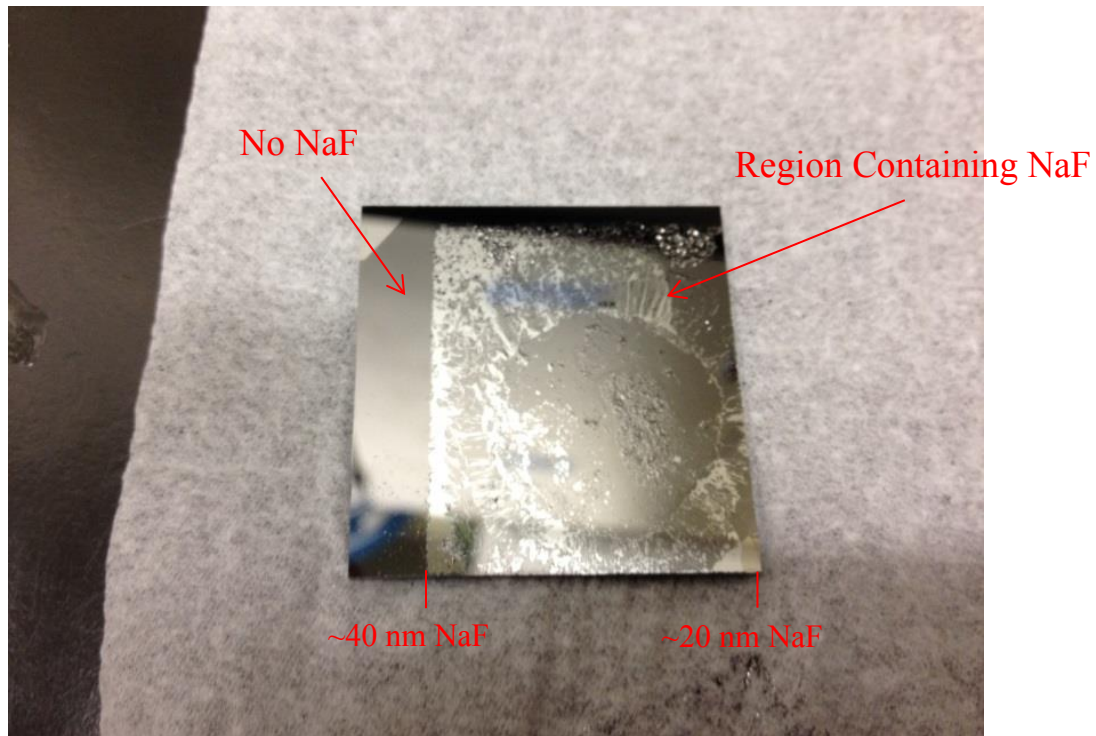


**Figure 4.7:** Demonstration of the dramatic effects water has on NaF treated precursors

immediate erosion of the region containing NaF, whereas the region without NaF remains unaffected.

This issue in delamination confined the experiments to NaF thicknesses of 40 nm and less. The delamination during annealing was attributed to improper chamber purging prior to beginning the heating cycle. Creating an optimal seal between the lid and the base of the graphite box minimized the rate Se vapor would flow out of the box but also reduced the rate at which air could be evacuated from the box during purging. In order to assure that all the air and therefore water vapor within the graphite box was being evacuated, the chamber was left to pump down overnight. This large extension of pump down was effective at removing any residual water vapor from the graphite box and the delamination issue during annealing was resolved.

To further investigate the quality of adhesion on films with NaF incorporation, a simple experiment was performed by scribing a line down the length of the film. The images contained in Fig. 4.8 were taken with an optical microscope along the length of the scribe mark. The first image in Fig. 4.8-a) corresponds to the scribe mark through a section of the film containing no NaF. It can be seen that the scribe only removed film that came in direct contact with the scribe tip which is an indication of good film adhesion to the substrate. The next image in Fig. 4.8-b) is of the scribe mark as it passed through the start of the NaF thickness gradient. There is a clear decrease in film adhesion as the scribe began pulling off whole sections of the film that were not in direct contact with the tip of the scribe. This trend continued for the entire length of the NaF gradient until in Fig. 4.8-c) when the NaF gradient began approaching 0 nm.

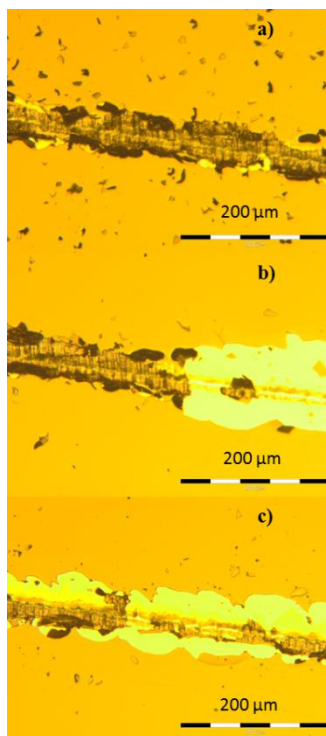


**Figure 4.8:** Images of scribe marks demonstrating the impact underlying NaF film has on film adhesion. a) region with no NaF b) region where NaF gradient starts c) region where NaF gradient reaches a minimum

#### 4.4 NaF Doping Analysis: Structure and Electronic Properties

To investigate the impact of sodium concentration on CZTSe film structure, SEM images of grain size were taken along the surface of the film and correlated with the approximate NaF thickness as measured prior to precursor deposition. The images in Fig. 4.9 were taken along the surface of the CZTSe every 3 mm and compared with the NaF thicknesses.

When comparing these images to the image of the film untreated with NaF in Fig. 4.2, it can be seen that NaF incorporation did result in increased grain size up to 1  $\mu\text{m}$ . The images do not exhibit any discernable pattern relating grain size to NaF concentration and the overall grain size is nonuniform across the entire surface of the film. This shows that a nonuniform concentration of NaF within the substrate will lead to nonuniform effects on the CZTSe. This suggests that if NaF is to be incorporated into the CZTSe manufacturing process, a high degree of uniformity within the NaF precursor must be obtained in order to avoid regional differences in structure and therefore device performance. However, the regions where the film was masked from NaF deposition do seem to exhibit less prominent effects of grain size growth. This suggests that the NaF mostly remained in the treated region and only transported to the ends of the film in very low concentrations.

The larger grains also seem to have precipitated to the surface. Figure 4.10 shows an SEM cross section image of the film analyzed in Fig. 4.9. This image shows that the film bulk is compact with no voids. To determine if the large surface grains differ in composition from the bulk, back scattered electron images and spot EDS analysis was acquired and can be seen in Fig. 4.11. The backscattered images show little change in

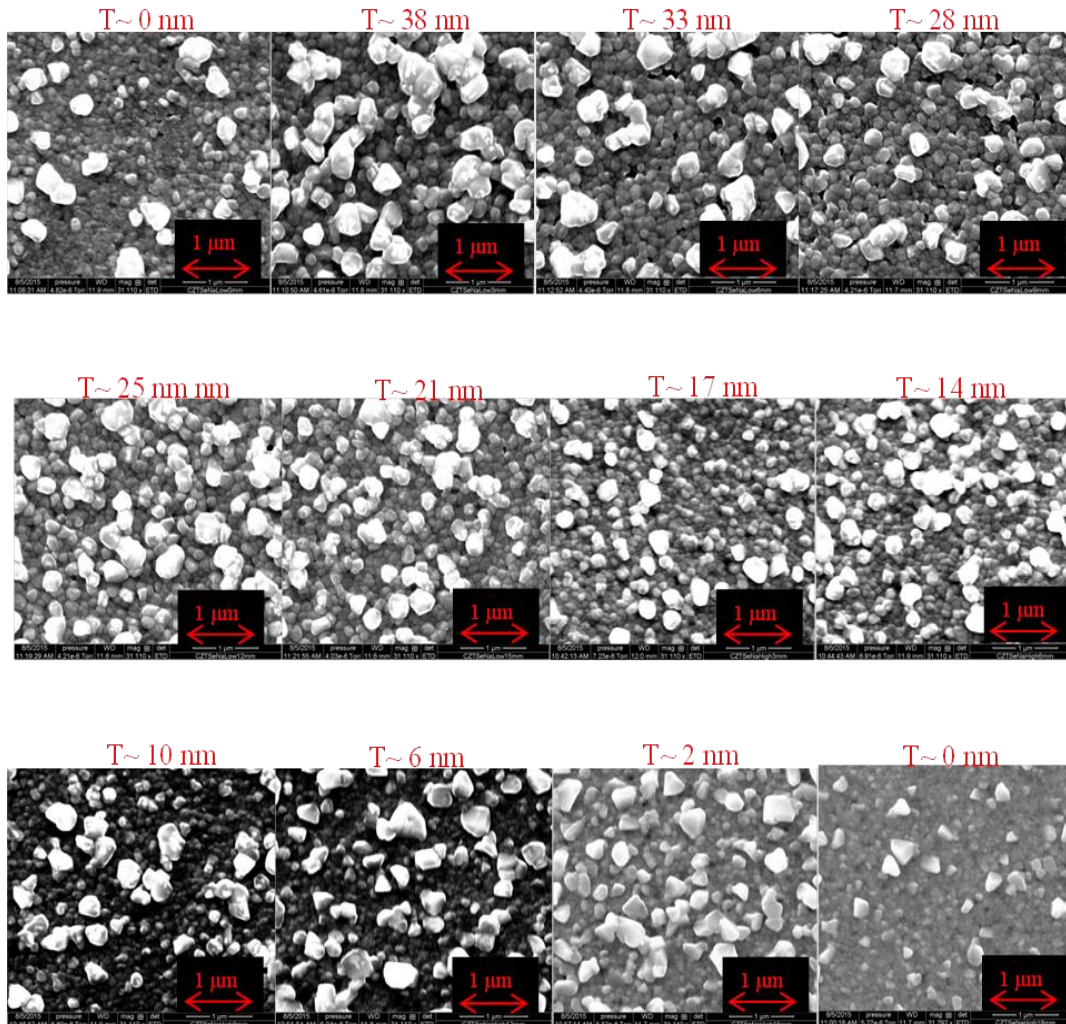


**Figure 4.9:** SEM images of grain size taken every 3 mm along the NaF composition gradient

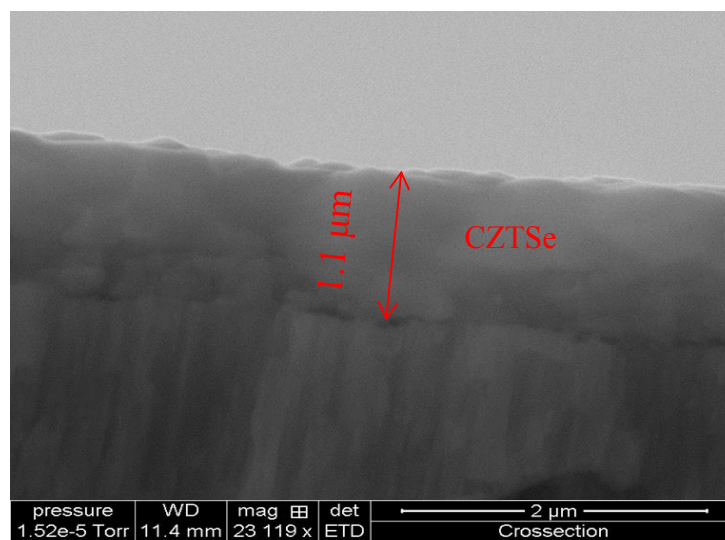
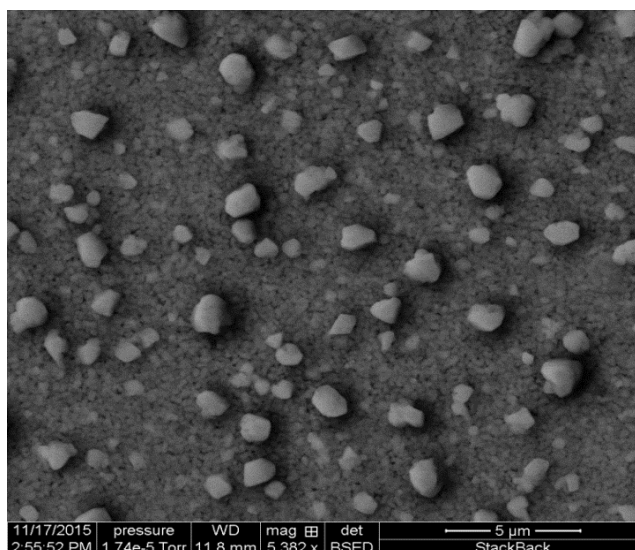


**Figure 4.10:** SEM image of cross section of CZTSe film doped with NaF gradient.





<b>Grain</b>		<b>Between Grains</b>	
<b>Element</b>	<b>At%</b>	<b>Element</b>	<b>At%</b>
Sn	11	Sn	9
Cu	21	Cu	18
Zn	12	Zn	10
Se	56	Se	63

**Figure 4.11:** Backscattered electron image of Na treated CZTSe with corresponding EDS. The image shows that the large surface grains are most likely the same phase as the underlying surface. Spot EDS data shows little difference in stoichiometry with the exception of less Se in large surface grains

contrast between the large surface grains and the smaller grains, suggesting that they are consistent in phase. However, spot EDS analysis shows a decrease in selenium content for the larger surface grains.

The XRD pattern for the sample treated with NaF is plotted with the untreated sample in Fig. 4.12. The XRD pattern shows that the incorporation of NaF had little effect on the structure of the film despite the formation of the large surface grains seen in Fig. 4.9. This suggests that these larger grains do not largely represent the bulk structure. The most interesting feature of the NaF treated film is the clear suppression of the MoSe<sub>2</sub> interfacial layer.

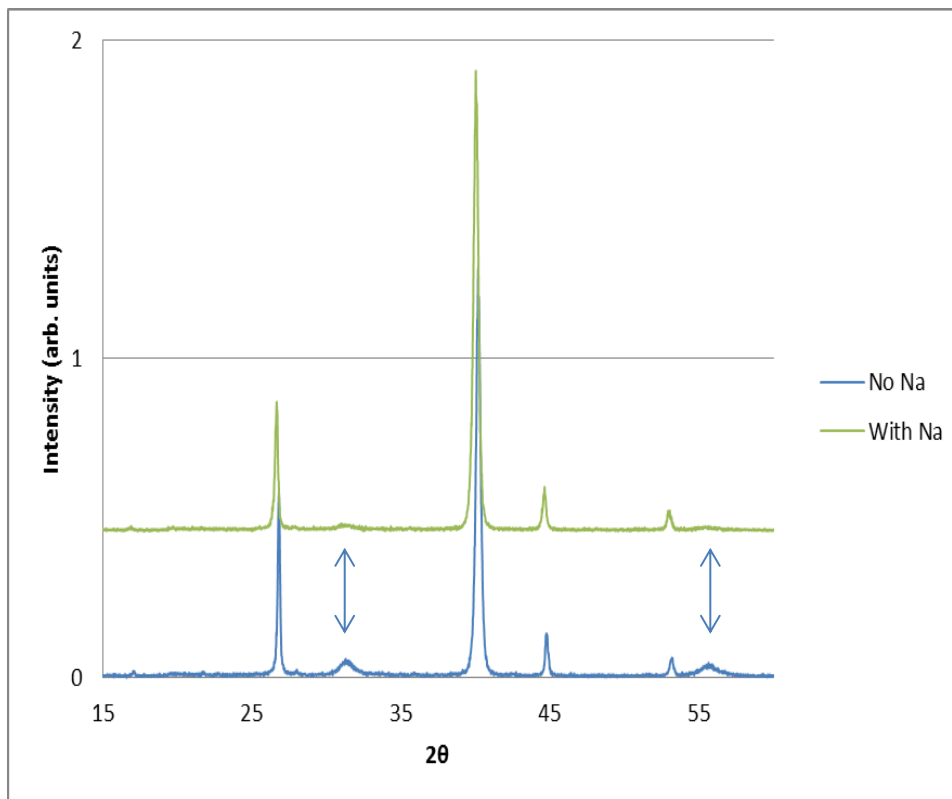


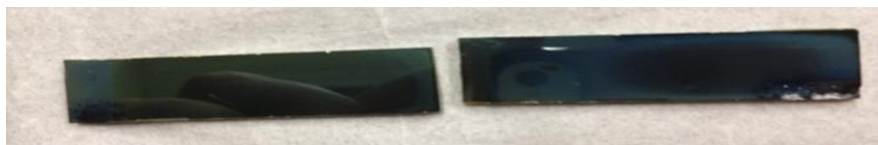
**Figure 4.12:** Comparison of XRD patterns from CZTSe treated with NaF (green) and without NaF (blue) showing the suppression of MoSe<sub>2</sub> (blue arrows)

The peaks corresponding to MoSe<sub>2</sub> are barely detectable, revealing that incorporation of NaF from the Mo substrate can suppress the formation of MoSe<sub>2</sub> which can be parasitic to device performance. The pattern also exhibits a slight shift in peak position. Calculating the peak shift shows that all peaks CZTSe and Mo are shifted by approximately 0.138. An equal shift on all peaks means the shift is most likely instrument/software induced as opposed to being the result of stress or compositional variation.

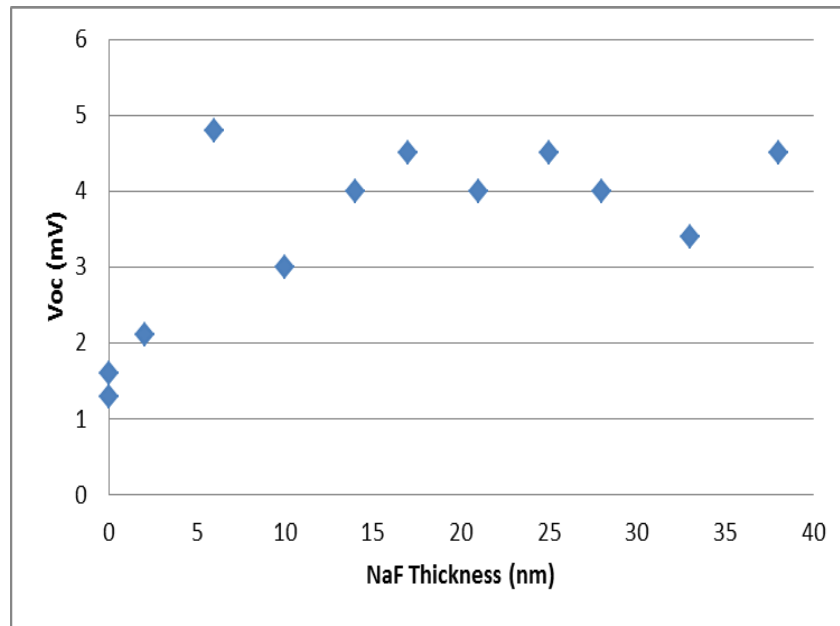
A further analysis was performed to investigate the possibility of a correlation between NaF concentration and grain boundary passivation. Grain boundaries are passivated by filling trap states with Na<sup>+</sup> ions that would otherwise act as recombination sites. Reducing

recombination sites increases excess minority carrier lifetimes which increases excess minority carrier density. The excess carrier density on both sides of the p-n junction creates an open-circuit voltage ( $V_{oc}$ ) which is related by equation (8) where  $\Delta n$  and  $\Delta p$  are excess carrier concentration,  $n_i$  is the intrinsic carrier concentration, and  $N_A$  is the dopant concentration. Equation (8) shows that an increase in excess carrier concentration produced by grain boundary passivation will result in an increase in  $V_{oc}$ .

In order to generate a  $V_{oc}$ , a p-n junction was formed. This was done by depositing a layer of CdS on the CZTSe using a chemical bath deposition and DC sputtering indium tin oxide (ITO). The chemical bath deposition consisted of 366 ml of deionized H<sub>2</sub>O, 62.5 ml of ammonium hydroxide NH<sub>4</sub>OH (28–30%), 50 ml of cadmium sulfate(0.015 M CdSO<sub>4</sub>), and 25 ml of thiourea (1.5 M NH<sub>2</sub>CSNH<sub>2</sub>) at 65° C. The resultant film is imaged in Fig. 4.13. The regions of the film were then scribed in regions corresponding to different initial NaF concentrations. The  $V_{oc}$  was measured for every region using a Keithly Series 2400 multimeter and micromanipulator probes under 1 sun illumination provided by a solar simulator. The results are plotted in Fig. 4.14 and show little correlation to initial NaF composition with the exception of the regions corresponding to zero initial NaF which show the lowest values of  $V_{oc}$ . The  $V_{oc}$  values are all very low, signifying that the CZTSe film is of poor electronic quality or the CdS/ITO depositions need to be further optimized.



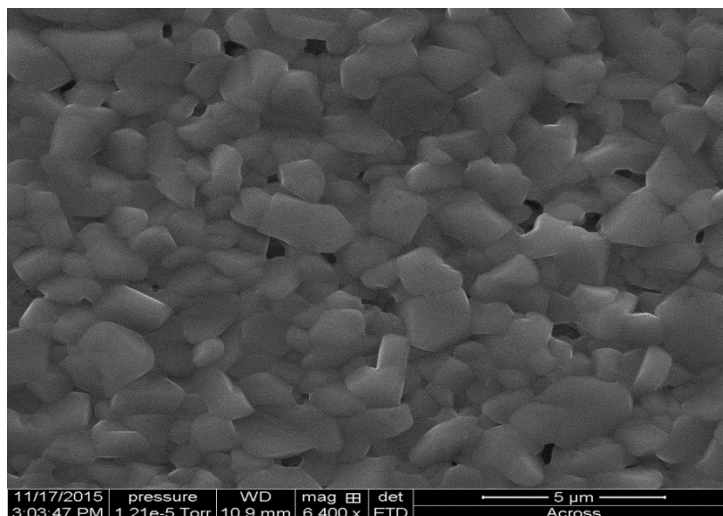
**Figure 4.13:** Images of NaF doped films after CdS/ITO deposition



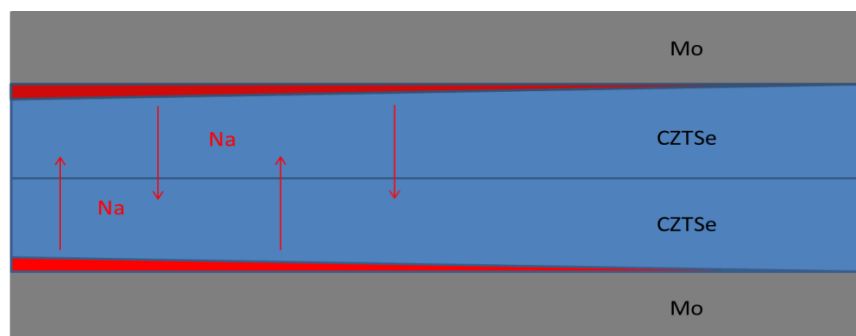
**Figure 4.14:**  $V_{oc}$  measurements taken along the NaF composition gradient

To make a comparison between the Na incorporation method through an NaF precursor layer and incorporation through diffusion from substrate, a sample was fabricated on soda lime glass (SLG) using the same process. Figure 4.15 contains an SEM image of the film surface after annealing. The image shows the film resulted in a different structure with a more uniform enhancement of grain growth.

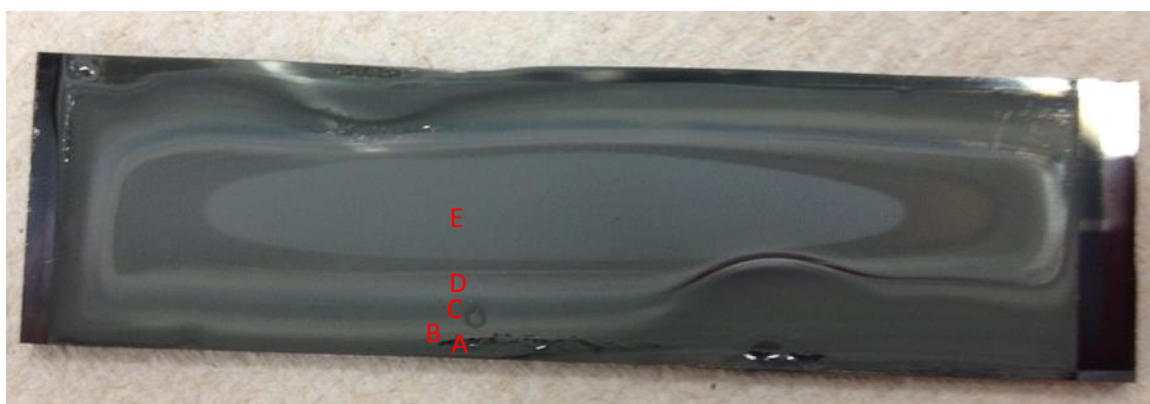
To further investigate the transport nature of the NaF during annealing, an experiment was performed which consisted of two NaF doped samples fabricated with the same recipe outlined in Chapter 3 except that the two samples were annealed “face to face” as illustrated in Fig. 4.16. The goal of this experiment was to minimize Na vapor loss due to an exchange between the two films rather than expansion into the volume of the annealing chamber. The image of the bottom film annealed in a face to face configuration is contained in Fig. 4.17 and shows nonuniformity in appearance across the surface of the film.



**Figure 4.15:** SEM image of CZTSe sample fabricated on soda lime glass substrate. Image shows larger and more uniform grain growth compared to CZTSe sample fabricated on sodium free eagle glass with NaF precursor layer

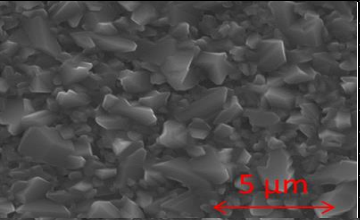
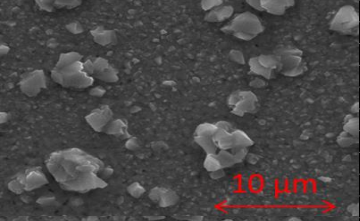
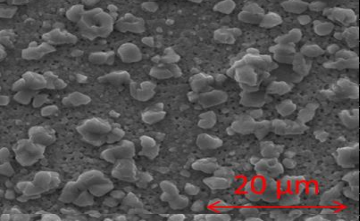
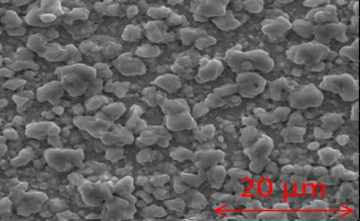
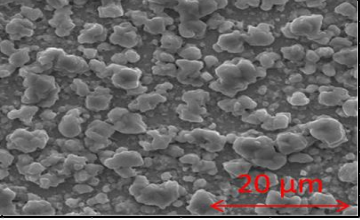


**Figure 4.16:** Illustration of face to face annealing technique preventing Na vapor loss



**Figure 4.17:** Image of CZTSe film doped with NaF gradient annealed “face to face” with another identical sample. The labels A-E correspond to the different spectral regions

To analyze the cause of the nonuniformity, SEM images and EDS were taken on each spectral region labeled in Fig. 4.17. The results of this analysis are tabulated in Fig. 4.18 which shows that the nonuniformity is due to a difference in the size and density of grains. The region corresponding to the edge of the film and labeled A shows grains up to 3.5  $\mu\text{m}$  in size. Moving in to the 2 mm to region B shows a change to larger grains up to 5  $\mu\text{m}$  in low density. Moving further in to regions C, D, and E shows further increase in grain size and density of enhanced grains which reaches a maximum at region E at the

<b>A</b>	<b>Element</b>	<b>At%</b>	
	Sn	11	
	Cu	18	
	Zn	9	
	Se	62	
<b>B</b>	<b>Element</b>	<b>At%</b>	
	Sn	12	
	Cu	18	
	Zn	11	
	Se	59	
<b>C</b>	<b>Element</b>	<b>At%</b>	
	Sn	12	
	Cu	21	
	Zn	11	
	Se	56	
<b>D</b>	<b>Element</b>	<b>At%</b>	
	Sn	13	
	Cu	22	
	Zn	11	
	Se	54	
<b>E</b>	<b>Element</b>	<b>At%</b>	
	Sn	13	
	Cu	22	
	Zn	12	
	Se	53	

**Figure 4.18:** SEM and EDS results for each spectral region A-E as labeled in Fig 4.14. These results show a dramatic increase in grain size and grain density from the edges towards the center

center of the film. The center region shows a large density of grains up to  $10\ \mu\text{m}$  which is a 10 fold increase in grain size from the film shown in Fig. 4.9 which was not annealed in the face to face configuration.

Figure 4.19 is a plot of EDS results for each region and they are expressed as Se to metals ratio and Zn to Sn ratio. The plot shows that the Zn/Sn ratio stays fairly constant around 0.9 from the edge to the center of the film while the Se content decreases from about 1.6 to 1.1. The decrease in Se content could be a side effect of the face to face annealing configuration restricting Se vapor from reaching the center of the film. This decrease in Se content may also be due to the change in film structure modulating the X-ray signal that is interpreted by the EDS software and not actually due to a change in composition.

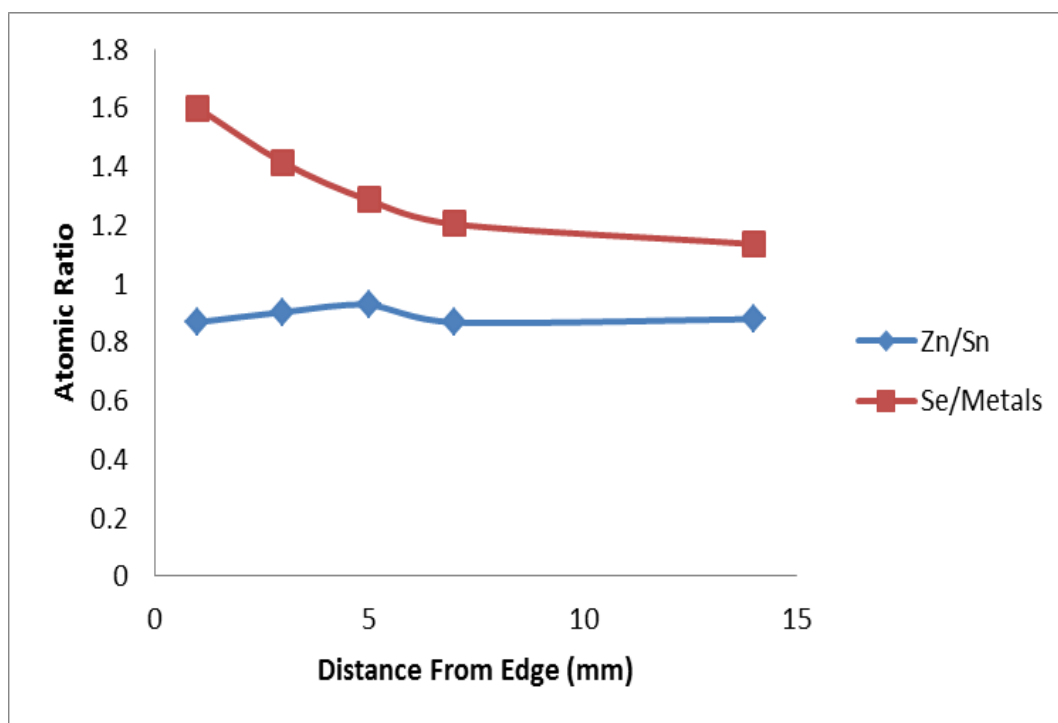


**Figure 4.19:** Plot of atomic ratios for each spectral region labeled in Fig. 4.14. It can be seen that Zn/Sn ratios remain nearly constant around 0.9 while Se content decreases from 1.6 at the edge to 1.1 in the center

This experiment verified the hypothesis that Na was escaping the film and the annealing environment in the vapor phase during annealing. Although annealing two CZTSe samples face to face prevented Na loss, it resulted in a film with a high degree of nonuniformity in structure across the width film. Since the nonuniformity does not occur across the length of the film, it is not likely due to the NaF thickness gradient. Further experiments need to be performed to determine whether the nonuniformity in grain growth kinetics across the width of the film is due to Na migrating and accumulating toward the center or if annealing in this configuration creates this effect regardless of the presence of Na.



## CHAPTER 5

### CONCLUSION

Thin film solar cells utilizing a  $\text{Cu}_2\text{ZnSnSe}_4$  (CZTSe) absorber layer show great potential for producing clean, affordable energy at terawatt level production. However, CZTSe devices have still not achieved this potential due to the discrepancy in device efficiency between the current record holding CZTSe cells and the expected theoretical efficiency. Overcoming this discrepancy has motivated research to further understand the growth and formation of the CZTSe phase as well as methods to enhance the fabrication process. In this study, the structural enhancement of CZTSe grains by the incorporation of Na during CZTSe fabrication was investigated using a combinatorial approach. Employing a combinatorial approach provides the potential to detect a correlation between Na concentration and the effects on film structure as well as gain insight into the transport properties of Na during the annealing process.

CuSe-ZnSe-SnSe precursors were grown on Mo coated alkali free glass substrates and then annealed in a graphite box contained in a steel vacuum chamber under an  $\text{N}_2$  atmosphere. Co-sputtering proved to be an effective method for depositing a uniform film with proper CZTSe stoichiometry. However, sputtering at 10 mTorr resulted in the formation of surface blisters during annealing. The blisters were determined to be the entrapment of argon gas during sputtering and were eliminated by reducing the sputtering

gas pressure to 6.8 mTorr. Films annealed in the graphite box at 580 °C for 20 minutes under a high Se vapor pressure provided Sepellets placed in the graphite box produced films containing predominantly CZTSe phase as detected by X-ray diffraction which was confirmed with Raman spectroscopy. The X-ray diffraction pattern also revealed the formation of a MoSe<sub>2</sub> interfacial layer approximately 12.5 nm. SEM images reveal the film consisted of nano-sized grains 300-400 nm in diameter. Optical absorption measurements determined the films displayed a high absorption coefficient ( $\alpha$ ) greater than 10<sup>4</sup> cm<sup>-1</sup> and a band gap ( $E_g$ ) approximately 1.0 eV which are characteristic values for CZTSe.

An investigation of the effects of incorporating Na during the annealing process was achieved by evaporating NaF onto the Mo coated substrate prior to precursor deposition using a constant withdrawal shutter. This process achieved a 60 mm long NaF film with a linear thickness gradient from 60nm to 0 nm which provided Na incorporation into the CZTSe during annealing with spatially varying concentration. This produced precursor films that were very sensitive to water and regions where the underlying NaF film was 40 nm and greater would immediately delaminate when exposed to the air. This sensitivity to moisture is attributed to the hygroscopic nature of NaF so humidity should be controlled when using NaF in the CZTSe manufacturing process and proper chamber purging must be administered to prevent film delamination during annealing.

SEM surface images of annealed CZTSe films treated with the NaF thickness gradient showed that every region of the film experienced increased grain growth up to 1  $\mu$ m regardless of the initial NaF concentration. This suggests that the underlying NaF layer film evaporates and transports to the entire surface of the film in the vapor phase.

However, the effects on areas corresponding to the regions of the film deposited outside the NaF gradient were much less pronounced. The enhancement of grain size was also not uniform throughout the entire film, suggesting either the annealing process was not brought to completion or the total Na concentration was not sufficient enough to supplement the entire film. There is also a possibility that evaporated Na may have left the annealing environment during annealing, leading to insufficient Na concentration.

Fabricating a film using the same process but utilizing soda lime glass as the substrate and source of Na offered a useful comparison between Na incorporation methods. Incorporation of Na by diffusion from substrate resulted in enhancement of grain growth with a much greater degree of uniformity. In summary, this experiment demonstrated that NaF incorporation from the underlying substrate can enhance CZTSe grain growth as well as suppress the formation of the  $\text{MoSe}_2$  at the back contact. However, it was also observed that the Na undergoes a high degree of vapor transport which can escape the annealing environment. This was confirmed by performing annealing in a face to face configuration which confined the Na vapor from escaping the annealing environment and lead to a nearly 10 fold increase in grain size. This experiment also demonstrated that a nonuniform incorporation of NaF will lead to nonuniform grain enhancement throughout the film. Because of this, it is suggested that the uniformity of the Na source incorporated during a manufacturing process must be maintained in order to produce films with uniform quality.

## REFERENCES

- [1] International Energy Agency . "2014 Key World Energy Statistics". pp. 6,24,28.May 5, 2014.
- [2] U.S. Energy Information Administration, International Energy Outlook 2013, Figure 2. World energy consumption by fuel type, 1990-2040.
- [3] International Energy Agency. "Snapshot of Global PV 1992-2014" Photovoltaic Power Systems Programme. 30 March 2015.
- [4] Qiang, Fu (2003). "Radiation (Solar)" In Holton, James R. Encyclopedia of atmospheric sciences 5. Amsterdam: Academic Press. pp. 1859–1863.
- [5] Fraunhofer ISE "Photovoltaics Report" 28 July 2014. Archived from the original on 31 August 2014. Retrieved 31 August 2014.
- [6] W. Wang, M.T. Winkler, O. Guanawan, T. Gokeman, T.K. Todorov, Y. Zhu, D.B. Mitzi, "Device Characteristics of cztsse thin-film solar cells with 12.6% efficiency". Adv. Denergy Mater. (2013).
- [7] G. Brammertz, M. Buffiere, S. Oueslati, H. Elanzeery, K. Ben Mossaoud, S. Sahayaraj, C. Koble, M. Meuris, J. Poortmans, "Characterization of defects in 9.7% efficient  $\text{Cu}_2\text{ZnSnSe}_4\text{-CdS-ZnO}$  solar cells", Appl. Phys. Lett. 103 (2013) 163904.
- [8] ASTM G173-03(2012), Standard Tables for Reference Solar Spectral Irradiances: Direct Normal and Hemispherical on  $37^\circ$  Tilted Surface, ASTM International, West Conshohocken, PA, 2012, [www.astm.org](http://www.astm.org).
- [9] B. Shin, O. Guanawan, Y. Zhu, Bojarczuk, S.J. Chey, S. Guha, "Thin Film solar cell with 8.4% power conversion efficiency using an earth-abundant  $\text{Cu}_2\text{ZnSnS}_4$  absorber", Prog. Photovolt, Res. Appl. 21 (2013) 72.
- [10] Calculated from data in "Reference Solar Spectral Irradiance: Air Mass 1.5" National Renewable Energy Laboratory. Sep 28, 2013.

- [11] W. Shockley and H. J. Queisser, "Detailed balance limit of efficiency of p-n junction solar cells," *Journal of Applied Physics*, vol. 32, pp. 510-519, March 1961.
- [12] J.L.C Daams, P. Villars, J.H.N. van Vucht, *Atlas of Crystal Structure Types for Intermetallic Phases*, (ASM International, Materials Park, Ohio, 1991), [CuFeSnS<sub>2</sub>] Vol. 3, pg. 4160; [Cu<sub>2</sub>ZnSnS<sub>4</sub>] Vol. 3, pg. 4164.
- [13] Haight, R., Barkhouse, A., Gunawan, O., Shin, B., Copel, M., Hopstaken, M. & Mitzi, D. B.(2011) Band alignment at the Cu<sub>2</sub>ZnSn(SxSe<sub>1-x</sub>)<sub>4</sub>/CdS interface. *Applied Physics Letters*, 98, 253502.
- [14] J.J. Scragg, *Conversion of Precursors into Compound Semiconductors Copper Zinc Tin Sulfide Thin Films for Photovoltaics*, Springer Berlin Heidelberg, 2011, pp. 59-110.
- [15] J.J. Scragg, T. Ericson, T. Kubart, M. Edoff, C. Platzer-Björkman, *Chemistry of Materials* 23 (2011) 4625-4633.
- [16] T. Tanaka, A. Yoshida, D. Saiki, K. Saito, Q. Guo, M. Nishio, T. Yamaguchi, *Thin Solid Films* 518 (2010) S29-S33.
- [17] Hultgren, R., Desai, P.D., Hawkins, D.T., Gleiser, M., Kelley, K.K., and Wagman, D.D., *Selected Values of Thermodynamic Properties of the Elements*, American Society for Metals, Metals Park, OH, 1973.
- [18] Philip Jackson, Dimitrios Hariskos, Roland Wuerz, Wiltraud Wischmann, Michael Powalla, Compositional investigation of potassium doped Cu(In,Ga)Se<sub>2</sub> solar cells with efficiencies upto 20.8%, *Phys.StatusSolidi(RRL)–Rapid Res.Lett.* 8(3)(2014)219–222.
- [19] M. Bodegård, L. Stolt, J. Hedström, The influence of sodium on the grain structure of CuInSe<sub>2</sub> films for photovoltaic application, Presented at the 12th European Photovoltaic Solar Energy Conference, Amsterdam, UK, 1994, p.1743.
- [20] T. Seward III, T. Vascott, "High Temperature Glass Melt Property Database for Process Modeling", The American Ceramic Society, Westerville, Ohio, 2005.
- [21] L. M. Mansfield , I. L. Repins , S. Glynn , M. D. Carducci , D. M. Honecker , J. W. Pankow , M. R. Young , C. DeHart , R. Sundaramoorthy , C. L. Beall and B. To "Sodium-doped molybdenum targets for controllable sodium incorporation in CIGS solar cells", *Proc. IEEE 37th IEEE Photovoltaic Spec. Conf.*, pp.003636 -003641 2011.

[22] Ingrid Repins, Carolyn Beall, Nirav Vora, Clay DeHart, Darius Kuciauskas, Pat Dippo, Bobby To, Jonathan Mann, Wan-Ching Hsu, Alan Goodrich, Rommel Noufi, Co-evaporated  $\text{Cu}_2\text{ZnSnSe}_4$  films and devices, *Sol. Energy Mater. Sol. Cells* 101(2012)154–159.

[23] Fermi Lab National Laboratory, “Materials for Ultra-high Vacuum” G. Lee, TM-1615, August 15 1989.

[24] Bras, P., Sterner, J., Platzer-Björkman, C. “Investigation of blister formation in sputtered  $\text{Cu}_2\text{ZnSnS}_4$  absorbers for thin film solar cells” *Journal of Vacuum Science and Technology A: Vacuum, Surfaces and Films*. Volume 33, Issue 6, 1 November 2015.